UiO Department of Mathematics
University of Oslo

Large Eddy Simulation of Turbulence in Helically Coiled Pipes: Effects of Mesh Strategy

Jacob Henrik Hudtwalcker
Master's Thesis, Autumn 2023

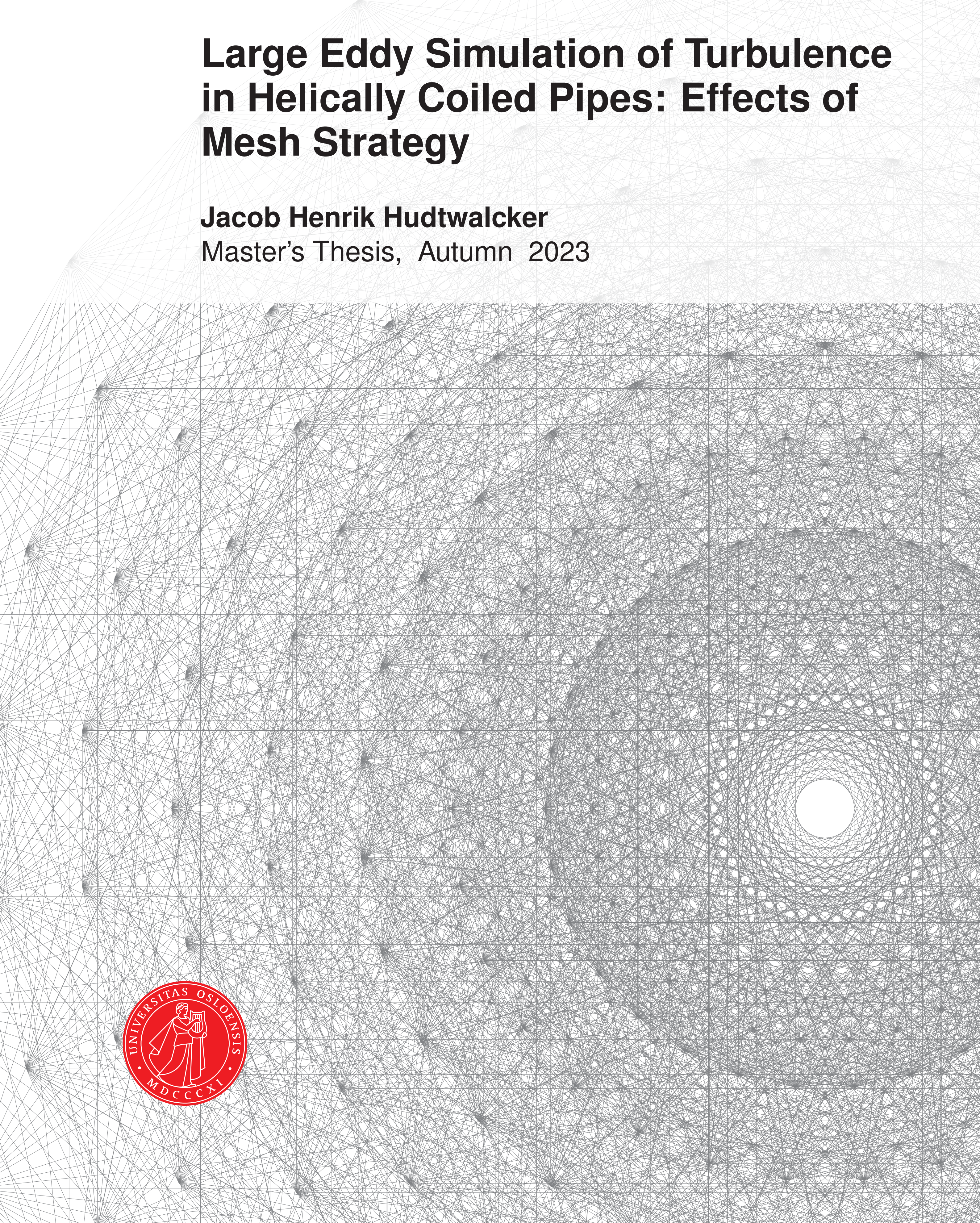

This master's thesis is submitted under the master's programme *Fluid Mechanics*, with programme option *Energy, environment and safety*, at the Department of Mathematics, University of Oslo. The scope of the thesis is 60 credits.

The front page depicts a section of the root system of the exceptional Lie group E_8, projected into the plane. Lie groups were invented by the Norwegian mathematician Sophus Lie (1842–1899) to express symmetries in differential equations and today they play a central role in various parts of mathematics.

Abstract

In this thesis we investigate the difficulties associated with the prediction of the behavior of turbulent flow in straight and helically coiled pipes, due to their prevalence in real world scenarios. To simulate the turbulent flow, we used Computational Fluid Dynamics with Large Eddy Simulation turbulence models. Due to the requirements on the mesh from the numerical code and turbulence models, we investigated which strategy for meshing of pipes provided the most accurate result, as well as the parameters of importance in mesh creation. To reduce the computational time needed for these simulations we compared the accuracy between coarse meshes with wall models accounting for small-scale phenomena, to meshes with a higher resolution where all scales of motion are resolved. Furthermore, we studied the effect the choice of turbulence model had on the development of turbulence in pipes. The results were compared to data from literature to examine the difference in accuracy between the techniques. The results from the aforementioned investigations were extrapolated to helically coiled pipes, where three different configurations were used to identify characteristics of turbulent flow within such geometries. We used fully turbulent flow from the results of the pipe simulations to insert accurate data to the inlet of the coils. The results showed a shift of the location of highest velocity towards the outer-wall, with a low velocity region appearing at the inner-wall. A spanwise pressure gradient was observed, inducing a centrifugal force on the flow, which caused secondary flow phenomena to occur.

We found that the central meshing parameter for straight- and helically coiled pipes was the skewness of the cells, and that a mesh with uniform size and shape is important towards the walls. Using wall models on a coarse mesh, gave satisfying results for a straight pipe, but may cause inaccuracies in more complex flow scenarios in the case of a helical coil. Moreover, the requirement of grid resolution from a straight- to helically coiled pipe seems to be non-transferable due to the increased complexity of the distribution and diffusion of turbulent kinetic energy.

Acknowledgements

First and foremost, I would like to thank my supervisors Mikael Mortensen and Kristian Valen-Sendstad for their guidance and support throughout this thesis. Their critical feedback based on their exceptional skills and knowledge of fluid mechanics and software, made the research and development process of the thesis natural.

I would also like to extend my deepest thanks to Kei Yamamoto for his academic support, insightful discussions and his willingness to provide advice.

Furthermore, I would like to express my gratitude to Terje Kvernes for his invaluable technical support, which without this thesis would not have been possible.

Lastly, I would like to thank my fiancée Sofia for all her support throughout the work on this thesis.

This thesis is dedicated to my mentor, teacher and friend Chi Huu Luong (1959-2022).

Contents

Abstract **i**

Acknowledgements **ii**

Contents **iii**

List of Figures **iv**

List of Tables **viii**

1 Introduction **1**

2 Theory of fluid mechanics and turbulence modelling **6**
- 2.1 Governing theory of fluid mechanics 6
- 2.2 Turbulence modelling 6
- 2.3 Dimensionless numbers 11
- 2.4 Numerical implementation 12
- 2.5 Wall-treatment in large eddy simulation 14

3 Methods of meshing and simulation **18**
- 3.1 Mesh-quality parameters 18
- 3.2 Creation of mesh geometry for pipes 20
- 3.3 Simulation setup for periodic turbulent flow in a pipe 22
- 3.4 Meshing of helically coiled pipes. 25
- 3.5 Simulation setup for the helically coiled pipes 27

4 Results and discussion **29**
- 4.1 Impact of mesh strategy on the solution 29
- 4.2 Results for periodic turbulent flow in a pipe 37
- 4.3 Results for turbulent flow in helically coiled pipes 48

5 Conclusion and future work **65**
- 5.1 Conclusion 65
- 5.2 Future work 67

Appendices **69**

A Wall shear stress in the O-grid pipe mesh **70**

B λ_2 criterion **71**

Bibliography **72**

List of Figures

1.1 Simplified helical heat exchangers for a tank. (a) shows an internal configuration, and (b) shows an external configuration. 2
1.2 Picture of the experiment indicating laminarization in helically coiled pipes from Viswanath et. al.[5]. The dye injection at the top of the coil quickly diffuses due to the turbulent flow, while the dye injection half way through the coil does not diffusive before the straight pipe outlet section, indicating laminar flow within the coil. 2
1.3 Different types of pipe meshes. (a) shows a typical O-grid mesh with five divisions with only hexahedral cells, (b) shows the pure hexahedral mesh from El Khoury et. al. [19] which has 12 divisions, and (c) shows the pure tetrahedral mesh from Yamamoto [11]. . . 4

2.1 Comparison of RANS, LES, and DNS from [21], showing the visual fidelity of the result. 7
2.2 Energy spectrum in wavenumber space for RANS, LES and DNS. 11
2.3 Diagram of a one dimensional mesh. 12
2.4 Plot of a turbulent boundary layer plotted with Law of the wall[38]. 14
2.5 Illustration of the wall model implementation from Mukha et. al.[32]. 16
2.6 Illustration of a resolved boundary layer mesh near the wall showing the increase in cell height. 17

3.1 Diagram of the face-area vector. 18
3.2 Cross sectional view of 4 different mesh types. (a) shows a classic O-grid mesh, (b) shows a automatically generated bell-curve O-grid, and (c) and (d) show the new meshes created with resolved and unresolved boundary layer respectively. 20
3.3 Schematic of the extruded profile for the new mesh. Here N_a is the number of the divisions in the azimuthal direction and N_i and N_m is the number of divisions between the turbulent boundary layer and the middle of the pipe. R is the radius of the pipe, while r is the radius to the refinement region near the wall. 21
3.4 Cross-sectional view of the meshes used for comparing results from WR- and WMLES to DNS data. (a) and (b) show the two different refinement levels used for WMLES, while (c) and (d) show the two refinement levels used for WRLES. 22

3.5 Side-view of the schematic for the periodic pipe. 23
3.6 Schematic of the longest coil, C3. The top left picture shows a side-view of the coil and the length of the straight outlet section, the top right picture shows a cross-sectional view of the coil with the measurement points for the pitch and the total height. The bottom picture shows a top-view of the coil where the radius of the coil R_c is the distance from the center point of the coil to the center point of the cross-section. 25
3.7 The three helical coil geometries used in the simulations. 27

4.1 Streaks in the time-averaged wall shear stress in the bell-curve mesh. (a) shows that the streaks in the whole domain, while (b) shows a close-up of the streaks which aling with the corner of the inner cuboid. 30
4.2 Streaks in the time-averaged wall shear stress in the WM-C mesh. The streaks have a randomly distributed pattern of streaks of the wall shear stress. 30
4.3 Lines used for sampling the TKE in bell-curve, O-grid, WR-C and WM-C meshes. 31
4.4 Sampled TKE in the four different meshes. The dashed line (- -) is the sampled TKE from the wall to center of the pipe through the corner of the central cuboid, while the filled line (-) shows the the TKE sampled along a line from the wall to the center of the pipe through the middle of a side of the central cuboid. Both the bell-curve (a) and the O-grid (b) show reduced TKE due to the non-uniformity of the boundary layer. 32
4.5 Skewness in three different meshes scaled by the same range. (a) shows the increased skewness in the bell-curve mesh extending from the inner cuboid, (b) and (c) show the reduced skewness in WM-C mesh classic O-grid mesh respectively. 33
4.6 Non-orthogonality in three different meshes scaled by the same range. (a) shows that the overall non-orthogonality is lower than in the proceeding configurations, while it has higher non-orthogonality in the boundary layer. (b) and (c) show that the non-orthogonality is reduced in the boundary layer while it is far greater in the inner cuboid compared to (a). 34
4.7 Velocity profiles of the mean (-) and the instantaneous (- -) colored by black for WALE, and red for Smagorinsky. (a) shows the velocity in the WR-C mesh after 350,000 timesteps, while (b) shows the velocity in the WM-C mesh. In both (a) and (b) the perturbations in the Smagorinsky diffused out, leaving an overlapping laminar profile for the mean and instantaneous velocity. 37
4.8 The profile of the mean normalized axial velocity four different simulations plotted against the results from El Khoury et. al. [19] and Yamamoto [11]. The horizontal dotted lines represent the three different regions in the turbulent boundary layer. The simulations using wall-models show good agreement with the DNS data in the log-law region, while the resolved simulations overpredict the profile. 39

4.9 Velocity profiles of the RMS velocities and the non-vanishing Reynolds stress in the four different simulations plotted against the results from El Khoury et. al. [19] and Yamamoto [11]. The simulations done with wall-models show better adherence to the DNS data from El Khoury et. al. [19] than the data from Yamamoto [11] and the WR-C simulation. 41
4.10 Normalized mean velocity profiles of the pipe with the (a) showing the mean velocity and (b) the root-mean square of the velocity. Both quantities are normalized by the bulk velocity and plotted with the data from Yamamoto [11]. The mean velocity profile in (a) shows good agreement to the data from Yamamoto [11], with no discernible differences between the four simulations. The RMS velocity profile shows that the profiles were overpredicted when compared to Yamamoto, and that the simulations using wall models create a more parabolic profile than that of the WR-F mesh. . . . 42
4.11 Vortices near the wall in WM-C and WR-F. In (a) The poor resolution is due to the low resolution of the mesh. From this result, the length of the pipe seemed to be sufficient to capture long turbulent structures along the wall. In (b) the higher resolution of the mesh gives greater insight into the small overlapping "Q-events" produced by the slow moving velocity streaks along the wall. . . . 43
4.12 Velocity streaks near the wall in the same timestep as Figure 4.11b. The velocity is colored by a scale with greater contrast to better visualize the pattern of the velocity streaks near the wall. 43
4.13 Illustration of the location of the slices used for analysis in the three different coil configurations. To emphasize the location of these slices, they were plotted with the time-averaged velocity magnitude. 48
4.14 Visualization of the mean velocity field in the three coils. (a) shows that C1 is too short for a stable secondary flow profile to develop, (b) shows that a stable secondary flow profile is established after two revolutions and (c) shows the stable secondary flow profile after two turns. 49
4.15 Streamlines of the breakdown of the secondary flow in C3 colored with the normalized mean velocity. As the secondary flow at the inner wall breaks down. 50
4.16 Time-averaged horizontal and vertical velocity profiles in C3 normalized with U_b. The velocity is plotted so that the left side shows the velocity at the inner wall of the pipe and the right side shows the velocity at the inner wall. The sampled lines are depicted in (A). The top plot (B) shows the vertical velocity profiles, sampled along the filled line (-), while the bottom plot (C) shows the horizontal velocity profile sampled along the dashed line (- -). The horizontal velocity shows that as the fluid flows through the coil, the velocity gradually increases at the outer wall, and decreases at the inner wall. 51

4.17 Pressure distribution in C3. The slices on the left-hand side (A) show the pressure in the sampled slices. The top plot on the right-hand side (B) show the decrease in the normalized pressure sampled along a horizontal line in the cross-sections depicted on the left. The orientation is such that the left side of the plot is towards the inner wall, while the right side is towards the outer wall. The overall pressure in the slice decreases as the fluid moves through the coil, reaching zero at the straight pipe section. The plot at the bottom right (C) shows the gradient of the pressure in the horizontal direction. The gradient reaches a stable value after one revolution. 52
4.18 Measurements of the spanwise pressure and pressure gradient in C1 and C2. (a) and (b) show that in C1, the coil was too short to give an accurate measurement of the pressure and the pressure gradient. (c) and (d) on the other hand, show that the pressure gradient reaches a stable value after one revolution in C2, in line with the findings in C3. The spanwise pressure gradient also shows similar characteristics to C3. 53
4.19 TKE in C1, C2, and C3 plotted such that all three figures share the same scale. The TKE in C1 in (a) exhibits different characteristics than the TKE in C2 and C3 due to the malformed geometry. (b) and (c) show that the TKE diffuses as the fluid moves through the coil, and increases again in the straight pipe outlet, which is inline with the findings from Viswanath et. al. [5]. 54
4.20 Captured energy spectra in C3. Due to the shifting of the location of the maximum velocity towards the outer wall and consequently the shifting of high TKE areas, the resolution of the mesh is not sufficient to capture 80% of the energy spectrum, leading to increased artificial diffusion. 55
4.21 Comparison of normalized TKE in C1, C2, and C3 to the DNS data from Yamamoto [11]. The three horizontal dotted lines represent each turn of the coil. It can be seen that the overall TKE is underestimated in each of the coils compared to similar coil geometries from Yamamoto [11]. 56
4.22 Schematic of two counter-rotating Dean vortices in the cross-section of a curved pipe [3]. 56
4.23 Line Integral Convolution (LIC) of the mean velocity in C3, showing the evolution of dean vortices throughout the coil. 57
4.24 Surface plots done using LIC and surface vectors of two instantaneous velocity profiles on the top, and the mean flow on the bottom. The instantaneous velocity shows the appearance of multiple vortices not captured by the mean velocity. 58
4.25 Resolution requirement due to the eddy size, borrowed from Lozano et. al. [57] 60
4.26 Energy of the turbulent eddies plotted over the wavenumber. k_c representes the cutoff-wavenumber i.e. the wavenumber of the smallest resolved eddy [59]. 62

A.1 Wall shear stress from Figure 3.2a. 70

List of Tables

3.1 Mesh parameters of the meshes used for comparing results from WR- and WMLES to DNS data. n_{cells} denotes the number of hexahedral cells in the mesh, NO_{max} and NO_{avg} the maximum and average non-orthogonality, SN the skewness, and y^+ is the height of the first cell in wall units 22
3.2 Boundary conditions for the periodic pipe. Spalding's Law of the wall was used for the wall-modelled simulations, while zero gradient was used for the wall-resolved simulations. 24
3.3 Numerical schemes for the periodic pipe. The temporal term is discretized with a second order backwards differencing scheme, and both the gradient and divergence were discretized by second order linear interpolation i.e. central differencing. The laplacian scheme is corrected using multiple non-orthogonality correction loops. . . . 24
3.4 Geometrical data for the helical coils 26
3.5 Boundary conditions for the three coil configurations. Spalding's Law of the wall was used for wall, the pressure at the outlet was set to zero, and the sampled data from the WM-C mesh was used as the Inlet condition. 28
3.6 Numerical schemes for the three coils. The temporal term is discretized with a second order backwards differencing scheme, and both the gradient and divergence were discretized by second order linear interpolation i.e. central differencing. The laplacian scheme is corrected using multiple non-orthogonality correction loops. 28

4.1 The domain-averaged values of the time-averaged wall shear stress in five different meshes. The analytical value is calculated from the target shear Reynolds number $Re_\tau = 180$, with the error reported in absolute percentage. The bell-curve shows a more accurate prediction when looking at the mean value than the O-grid, which hides the local inaccuracies in the bell-curve from the visual representation. 31
4.2 Absolute error in percentage in the shear Reynolds number in the four different simulations when compared to the target value from El Khoury et. al. [19]. The simulations with wall models show an overprediction of the target value, while the resolved simulations show an underprediction. WM-C is overall the most accurate using this metric. 38

4.3 Absolute error in percentage in the normalized shear velocity in the four different simulations when compared to the target value from El Khoury et. al. [19]. The simulations with wall models show an overprediction of the target value, while the resolved simulations show an underprediction. WM-C is overall the most accurate using this metric. 38
4.4 Difference in curvature κ and torsion τ in percentage between C1, C2, and C3. Negative percentage indicates a decrease while a positive percentage represents increase. The increase of curvature is greater between C1 and C2, than between C2 and C3, while the decrease in torsion between C1 and C3 is greater than that of C2 and C3. 63

CHAPTER 1

Introduction

In both engineering and science, the motion and properties of fluids is an important subject. In science, research into the mathematical formulation and physical interpretation of fluid motion can be applied to a variety of fields. From large off-shore wind parks, to the flow of blood in arteries. Furthermore, being able to capture accurately how a fluid behaves, is crucial for making design decisions in engineering, as the fluid can be the source of failure and also give insight into the efficiency of the design.

A central aspect to fluid flow in many real world applications, is the chaotic motion of turbulence. The irregular and highly complex fluid motion in turbulent flow presents a challenge for the predictability of fluid flows as well as the accuracy of measurements and computer simulations. Turbulence often occurs in high velocity scenarios where smooth laminar flow breaks down due to increased shear stress within the fluid, or due to obstacles in the flow field. Turbulent flow features favorable characteristics such as increased mass and heat transfer, as well as enhanced mixing of the fluid, which further increases the need for predictability. These are favourable properties in a variety of industrial applications such as chemical reactors and heat exchangers. One such heat exchanger configuration which has interesting effects on turbulent flow is helically coiled pipe heat exchangers.

Helically coiled pipes are used in a variety of applications, from medical to nuclear-engineering, as outlined in the extensive report by Vashisth et al. [1]. They are commonly used as both external, and internal heat exchangers for pipes, tanks, and components in nuclear reactors. The compact structure of a helical coiled heat exchanger makes it a suitable choice for applications where space is limited, exemplified in Figure 1.1. Furthermore, it features a much higher heat transfer coefficient than straight pipe heat exchangers [2]. This is due to the secondary flow induced by the centrifugal force induced by the fluid moving through the helix, which causes the fluid to mix in a more efficient matter compared to a straight pipe. These secondary flows are called Prandtl's secondary flow of the first kind, which superimpose counter-rotating Dean vortices, first presented by W.R Dean in 1927 [3]. One other notable property of helically coiled pipes is the laminarization of turbulent flow. This was first shown experimentally in helical coils by Taylor in 1929[4], where it was shown that turbulent flow entering a helix becomes laminar, and that the flow in a helix stays laminar for a much higher Reynolds number than in a straight

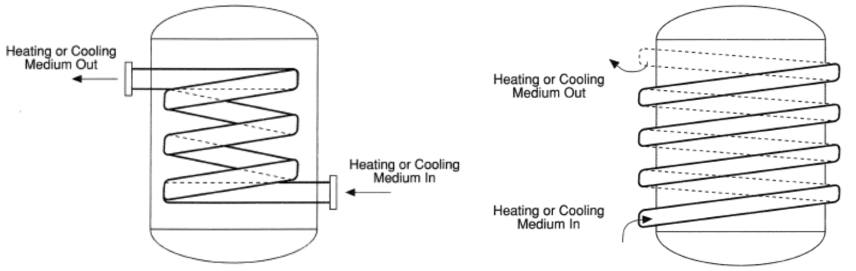

(a) Internal heat exchanger (b) External heat exchanger

Figure 1.1: Simplified helical heat exchangers for a tank. (a) shows an internal configuration, and (b) shows an external configuration.

pipe [5] [4] [6]. Furthermore, Viswanath et. al. [5] showed that turbulent flow entering a coil can become laminar inside the coil, while becoming turbulent again downstream of a straight pipe outlet. This effect can be seen in Figure 1.2 where the dye injected in the top of the coil quickly diffuses, which indicates a turbulent flow, however when injecting a secondary dye at the fourth coil, the dye does not diffuse which indicates laminar flow. Viswanath et. al. [5] noted that further downstream of the outlet, which is not pictured, the dye diffuses, indicating that the flow has become turbulent.

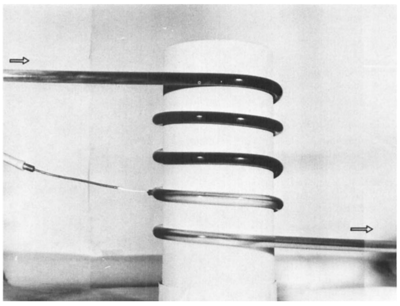

Figure 1.2: Picture of the experiment indicating laminarization in helically coiled pipes from Viswanath et. al.[5]. The dye injection at the top of the coil quickly diffuses due to the turbulent flow, while the dye injection half way through the coil does not diffusive before the straight pipe outlet section, indicating laminar flow within the coil.

To study the turbulent motion within a helical coil or a straight pipe, experiments and/or numerical simulations of fluid motion, called Computational Fluid Dynamics (CFD), can be used. There have been numerous studies done on turbulent flow in helical coils [5] [7] [6] and curved pipes [8] [9], but most have been done experimentally. There are however also studies done numerically [7] [10] [11], but they have either been performed using Reynolds Averaged Navier-Stokes (RANS) turbulence models [7] [10], which are known to not be robust for geometries with complex flow and turbulent decay [12] [13], or Direct Numerical Simulation (DNS) [11] which can be prohibitively computationally expensive.

The chaotic motion of turbulent flow is hard to capture numerically, thus have many mathematical models and techniques been developed for CFD. Turbulent periodic flows in simplistic geometries such as a channel or a backwards-facing step, are often used as a benchmark for testing and comparing data in numerical simulations. This is especially apparent by the geometries used in NASA's "*Turbulence Modelling Resource database*" [14] and the prevalence of the channel geometry in literature. Pipes, although simplistic in their design, are often not included in these studies, as the meshing techniques involved may be more labour heavy, since many numerical codes perform better on hexahedral cells which, depending on the code and numerical method used, may not be able to account for the added numerical diffusion due to the malformed cells in the pipe. This is due to the complexity of maintaining the shape of a hexahedral cell, while not losing the curved wall of the pipe. As pipes are directly applicable to real world geometries, it is of interest to see if a high grade of accuracy on these types of geometries can be reached using a Large Eddy Simulation (LES) turbulence model, while keeping the cell count low.

There have been performed studies on pipe-meshes for turbulent flows, most notably from Martins et. al. [15] who performed a parametric study on 92 different meshes, from Ballesteros et. al. [16] who use three different types of pipe meshes to validate against experimental data and from Hernandez et. al. [17] who investigate the accuracy of three types of hexahedral meshes for pipes. It is however important to note that these studies all use the Finite Volume Method (FVM), as the form of meshing techniques vary widely between numerical techniques and solvers. The common theme for pipe meshes created for FVM is the splitting of the mesh into five separate parts, one being the core of the pipe and the remaining four being created identical to form the outer part of the pipe. There are many different ways to form this geometry, with the most common having a rectangular cuboid as the core, often referred to as a butterfly or O-grid type mesh as seen in Figure 1.3a [16] [17]. This type of hexahedral mesh was shown to give the most accurate result when compared to a polar, H-grid and unstructured grid using FVM [17]. Meshes created for the spectral element method seem to often split the geometry into many more parts [18] [19] as seen in Figure 1.3b where the mesh is split up into 12 parts. Whereas meshes using the finite element method only use tetrahedral cells split into one region for the viscous sub-layer and one for the inner-region, as in the case of Yamamoto [11] depicted in Figure 1.3c.

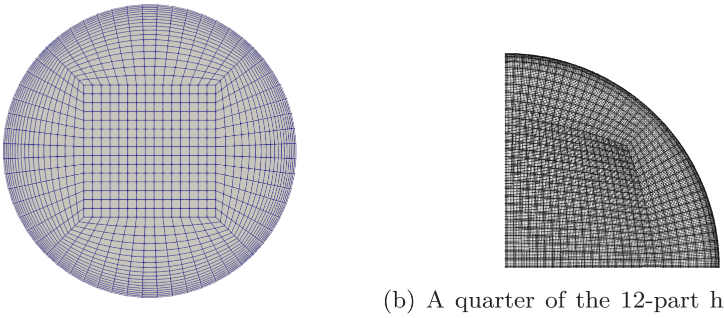

(a) Hexahedral O-grid Mesh.

(b) A quarter of the 12-part hexahedral mesh from El Khoury et. al. [19]

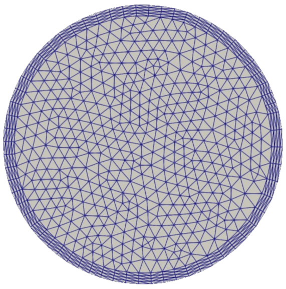

(c) Pure tetrahedral mesh from Yamamoto [11]

Figure 1.3: Different types of pipe meshes. (a) shows a typical O-grid mesh with five divisions with only hexahedral cells, (b) shows the pure hexahedral mesh from El Khoury et. al. [19] which has 12 divisions, and (c) shows the pure tetrahedral mesh from Yamamoto [11].

The optimal mesh geometry for a pipe using FVM is still not well documented in literature. Employing more contemporary techniques such as automatic generation and taking inspiration for meshes used in other numerical methods, could give insight into the characteristics of an improved mesh geometry, building on the findings from Hernandez et. al. [17], however for use with LES models, where uniformity of cell size is a central metric for accuracy.

In this thesis we will investigate how we can optimize LES simulations in complex flow scenarios, considering factors such as mesh strategy and resolution, wall modeling accuracy, and the impact of complex geometries. We will use the FVM based framework OpenFOAM (Open-source Field Operation And Manipulation) from ESI Group [20] to first look at three different pipe mesh geometries; one classical O-grid, one automatically generated and lastly a new one which has a rounder central cuboid than the classic O-grid. We will look at which mesh parameters have the most effect on the accuracy and their ability to maintain cell uniform. The mesh that performs best out of the three, will then be used for further study of the trade off between accuracy and computational cost of coarse meshes created for simulations with wall models and meshes without wall models that features a refinement region towards the wall. Furthermore, we will compare two prevalent LES models to compare the difference in performance for a geometry enclosed in walls such as pipes. The results will be compared against DNS data generated with the finite element method from Yamamoto [11], and DNS data generated with the spectral element method from El Khoury et. al. The results from the best performing mesh configuration will then be used as input data to simulate fully turbulent flow within three different helically coiled pipes. We will investigate the effect the geometry has on the turbulence within the coil, the effect of the centrifugal force and the Dean vortices and other secondary flow phenomena. The findings will be compared with literature where the same characteristics have been correlated with the performance of helically coiled heat exchangers.

CHAPTER 2

Theory of fluid mechanics and turbulence modelling

2.1 Governing theory of fluid mechanics

The Navier-Stokes equation Equation (2.1) is the equation used to describe the characteristics of fluid flow along with the continuity equation Equation (2.2).

$$\rho\left(\frac{\partial u_i}{\partial t} + u_j\frac{\partial u_i}{\partial x_j}\right) = -\frac{dp}{dx_i} + \mu\frac{\partial^2 u_i}{\partial x_j \partial x_j} + \rho g_i, \tag{2.1}$$

$$\frac{\partial u_i}{\partial x_i} = 0. \tag{2.2}$$

Here ρ is the density, u_i is a component of the velocity vector $\vec{u}$, t is time, g_i is the component of the body-force vector $\vec{g}$ which represents the acceleration due to gravity or other external forces, p is the pressure and μ is the dynamic viscosity coefficient.

The individual terms in Equation (2.1) are often referred to separately, from left to right, as the transient term, the convective term, the pressure gradient, the viscous term, and the bodyforces. If the fluid is incompressible (i.e. constant density is assumed) and it is unaffected by external forces, we can rewrite Equation (2.1) by dividing by the density and removing the external body forces term to get the incompressible Navier-Stokes equation

$$\frac{\partial u_i}{\partial t} + u_j\frac{\partial u_i}{\partial x_j} = -\frac{1}{\rho}\frac{\partial p}{\partial x_i} + \nu\frac{\partial^2 u_i}{\partial x_j \partial x_j}. \tag{2.3}$$

Here ν is the kinematic viscosity.

2.2 Turbulence modelling

One of the main areas of research in the fluid dynamics field, is the modelling of turbulence. It emerges out of the need to find ways to handle the non-linearity in the convection term in Equation (2.1) mathematically. Turbulence modelling can be split into three main categories; RANS, DNS, and LES. As seen in Figure 2.1, these three different methods give increasing resolution of the turbulent structures when simulating a turbulent jet. While there exist many more, such as Unsteady Reynolds Averaged Navier-Stokes Equations and Detached Eddy Simulations, these three are the most prevalent ones and represent the fundamental ideas on which most models are based.

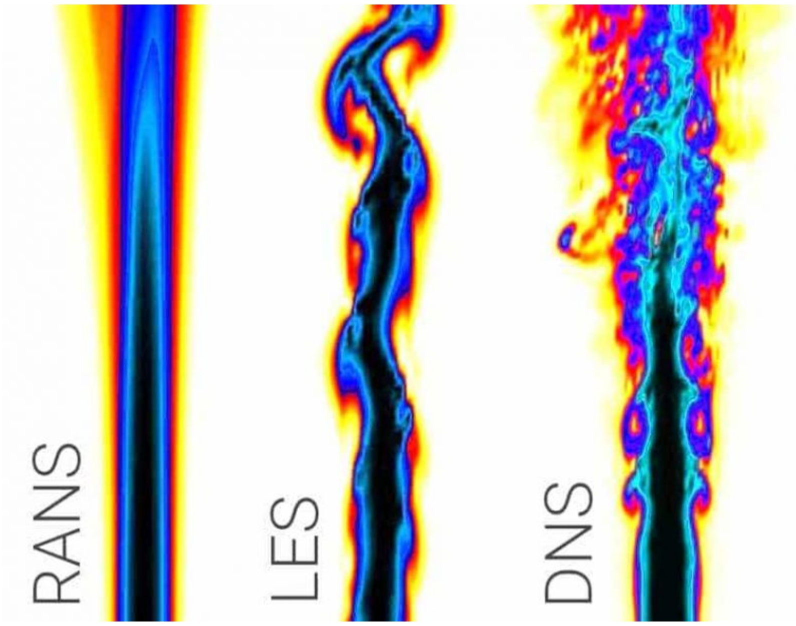

Figure 2.1: Comparison of RANS, LES, and DNS from [21], showing the visual fidelity of the result.

The RANS models are based on Reynolds Averaging [22] of Equation (2.1) [13], where the transported quantity is split into its temporal mean and temporal fluctuating components such that the apparent stresses, called Reynolds stresses, from the fluctuating velocity components becomes the only term that requires approximation from a mathematical model. These mathematical models vary between applications.

DNS on the other hand, solves the Navier-Stokes equations directly, without using any turbulence models [13]. DNS requires a very refined computational domain, such that all the motions of the fluid are solved down to the smallest scale. This makes DNS unfeasible for moderate to high Reynolds number applications [23].

LES turbulence modelling is the midpoint between the two former methods in terms of computational cost and accuracy. In LES turbulence modelling, a filter is used to filter out turbulent eddies of a certain size. The filtering process can either be explicit or implicit, with the latter being the most widely used due to the reduced complexity. In implicit filtering the cutoff width is calculated from a characteristic length of a computational cell. Typically as the cubic root of the volume or the maximum cartesian displacement. The eddies large enough to be resolved by the grid are calculated directly as in DNS, while the eddies that get filtered out are calculated with different LES turbulence models. The models account for the additional diffusion in the flow field due to the transfer of energy from the resolved to the unresolved eddies. As a general requirement, a mesh for LES should be sufficiently fine enough as to at least capture 80% of the energy-cascade [23], while the remaining 20% is accounted for by a LES turbulence model.

Large eddy simulation

There are two methods of filtering in LES; Explicit filtering and implicit filtering. Explicit filtering is often used to derive the LES equations [24], while implicit filtering arises naturally in a computational domain where the eddies are smaller than the cell size. Implicit filtering[25] is the most commonly used technique in FVM codes for turbulence models where only one level of filtering is required. The cutoff width $\Delta = \sqrt[3]{V_{cell}}$ raises naturally due to the formulation of the fluxes when using FVM [26]. Filtering of a transported quantity ϕ_i gives

$$\phi_i = \bar{\phi_i} + \phi', \tag{2.4}$$

where $\bar{\phi_i}$ is the resolved part and ϕ' is the unresolved part. Implicit filtering of the Navier-Stokes equations gives

$$\frac{\partial \bar{u}_i}{\partial t} + \bar{u_j}\frac{\partial \bar{u}_i}{\partial x_j} = -\frac{1}{\rho}\frac{\partial \bar{p}}{\partial x_i} + \nu\frac{\partial^2 \bar{u}_i}{\partial x_j \partial x_j} + \frac{\partial \tau_{ij}}{\partial x_j}, \tag{2.5}$$

$$\frac{\partial \bar{u}_i}{\partial x_i} = 0, \tag{2.6}$$

where

$$\tau_{ij} = \overline{u_i u_j} - \bar{u}_i \bar{u}_j, \tag{2.7}$$

is the Sub-Grid scale Stresses (SGS) from the interactions of the unresolved eddies that are filtered out. While these can be separated into resolved, unresolved and cross-scale stresses [27], they are usually lumped together in CFD codes using FVM [13]. The SGS tensor τ_{ij} is modelled using the Boussinesq eddy viscosity hypothesis[28] as

$$\tau_{ij} = -2\nu_t \bar{S}_{ij} + \frac{1}{3}\tau_{ii}\delta_{ij}, \tag{2.8}$$

where ν_t is the turbulent kinematic viscosity and $\bar{S}_{ij}$ is the strain-rate tensor. In numerical codes, the transfer of the kinetic energy from the resolved scale to the sub-grid scale is introduced by the turbulent kinematic viscosity ν_t. To model ν_t we are going to use the Smagorinsky model [29] and the Wall Adapting Local Eddy-viscosity (WALE) model [30].

The Smagorinsky turbulence model

The Smagorinsky turbulence model was first proposed by Joseph Smagorinsky in 1963 [29], and serves today as a basis for many SGS models. Smagorinsky conceived the model to be used to model the relation between the large and small scales in meteorological flows such as cyclones. The model assumes that the eddies are isotropic, such that they can be represented with a characteristic length l_0 and velocity U_0 to get the correct units for the kinematic viscosity as $m^2 s^{-1}$. Smagorinsky proposed this length to be a fraction of the filter size such that l_0 represents the size of an unresolved eddy that has the same amount of turbulent kinetic energy as if we were to take an average of the turbulent kinetic energy of all the unresolved eddies in one cell. As this eddy is smaller than the cell size, it is multiplied by a constant $C_s \in \langle 0, 1 \rangle$. This gives

$$l_0 = C_s \Delta, \tag{2.9}$$

where C_s is the Smagorinsky constant and Δ is the filter size. The characteristic velocity is calculated by the magnitude of the filtered strain rate tensor $\bar{S}_i j$ multiplied by $\sqrt{2}$, due to the result of the magnitude of the strain rate tensor, such that the characteristic velocity is accounted for in all directions

$$U_0 = C_s \Delta \sqrt{2} |\bar{S}_{ij}| = C_s \Delta \sqrt{2 \bar{S}_{ij} \bar{S}_{ij}}. \tag{2.10}$$

We then get the equation for the turbulent kinematic viscosity ν_t as

$$\nu_t = (C_s \Delta)^2 \sqrt{2 \bar{S}_{ij} \bar{S}_{ij}}. \tag{2.11}$$

The value of C_s was first shown by Lilly analytically to be $C_s \approx 0.173$[31], but has since then changed to many different values depending on the author of the paper[23] or the version of the CFD Software used.

The Wall Adapting Local Eddy-viscosity turbulence model

The WALE turbulence model [30] was chosen as the best turbulence model for this thesis as it was conceived as an improvement over the Smagorinsky [29] model for wall-bounded flows and was also shown to work well with the employed wall-model library [32]. Since the Smagorinsky model estimates the eddy-viscosity ν_t based on the local strain rate, ν_t is non-zero whenever there is a velocity gradient present, but this should not be the case near walls where the turbulent fluctuations are damped, causing ν_t to be zero. The WALE model counteracts this by defining an operator $\mathcal{L}$ made up of both the rotation tensor $\bar{\Omega}_{i,j}$ and the strain tensor $\bar{S}_{ij}$ such that viscosity goes to zero at the wall. This operator is constructed such that it is easily evaluated on any type of computational grid.
In WALE, ν_t is modelled by

$$\nu_t = (C_w \Delta)^2 \mathcal{L}. \tag{2.12}$$

Here

$$C_w^2 = C_s^2 \frac{\langle \sqrt{2} \left(\bar{S}_{ij} \bar{S}_{ij} \right)^{3/2} \rangle}{[\bar{S}_{ij} \bar{S}_{ij} \mathcal{L}]}, \tag{2.13}$$

where C_w is a model constant, C_s is the Smagorinsky constant [29] and

$$\mathcal{L} = \frac{\left(W_{ij}^d W_{ij}^d \right)^{3/2}}{\left(\bar{S}_{ij} \bar{S}_{ij} \right)^{5/2} + \left(W_{ij}^d W_{ij}^d \right)^{5/4}}. \tag{2.14}$$

Here W_{ij}^d is the tensor

$$W_{ij}^d = \bar{S}_{ik} \bar{S}_{kj} + \bar{\Omega}_{ik} \bar{\Omega}_{kj} - \frac{1}{3} \delta_{ij} \left[\bar{S}_{mn} \bar{S}_{mn} - \bar{\Omega}_{mn} \bar{\Omega}_{mn} \right]. \tag{2.15}$$

Turbulent kinetic energy in large eddy simulation

The turbulent kinetic energy (TKE) is a central parameter in LES. It is used to calculate how much of the energy spectrum is captured, and thus can be used to judge the validity of a LES simulation, as ν_t is essentially a parameter to represent the transfer of energy from the resolved field, to the unresolved field. Furthermore, an equation for the unresolved TKE is used to close the last term on the right-hand side in Equation (2.7) as it is still unaccounted for. The unresolved TKE can be calculated from τ_{ii} recognizing that

$$k_{sgs} = \frac{1}{2}\tau_{ii} = \frac{1}{2}(\overline{u_i u_i} - \bar{u_i}\bar{u_i}). \tag{2.16}$$

Additionally, the calculation of ν_t in CFD codes which has multiple turbulence models are usually done with a one-equation eddy viscosity model [33]

$$\nu_t = C_k \Delta \sqrt{k_{sgs}}, \tag{2.17}$$

where C_k is a constant, such that we can rewrite Equation (2.7) as

$$\tau_{ij} = -2 C_k \Delta \sqrt{k_{sgs}} \bar{S}_{ij} + \frac{2}{3} k_{sgs} \delta_{ij}, \tag{2.18}$$

thus the model is closed if k_{sgs} can be calculated.

The calculation of k_{sgs} depends on the turbulence model used, as Equation (2.17) must be correctly represented by its respective models. In the Smagorinsky model, k_{sgs} is calculated by an assumption of local equilibrium, arriving at the equation for incompressible flows

$$k_{sqs} = \frac{C_k}{C_\epsilon} \Delta^2 |\bar{S}_{ij}|, \tag{2.19}$$

where C_ϵ is a constant. For the WALE model, k_{sgs} is calculated by

$$k_{sgs} = \left(\frac{C_w^2 \Delta}{C_k} \right)^2 \left[\frac{(W_{ij}^d W_{ij}^d)^3}{\left((\bar{S}_{ij} \bar{S}_{ij})^{5/2} + (W_{ij}^d W_{ij}^d)^{5/4} \right)^2} \right], \tag{2.20}$$

thus giving the same equation as in Section 2.2. To calculate the mean total TKE k_{tot} we first split it into its resolved and unresolved part respectively. The resolved part of the TKE k_{res} is calculated by performing Reynolds averaging on resolved velocity field such that

$$\bar{u_i}'' = \langle \bar{u_i} \rangle - \bar{u_i}, \tag{2.21}$$

where $\bar{u_i}''$ is the time-fluctuating component of the resolved velocity and $\langle \bar{u_i} \rangle$ is the mean resolved velocity in time. By taking the mean of the fluctuating component we can calculate the resolved TKE by

$$k_{res} = \frac{1}{2} \langle \bar{u_i}'' \rangle^2, \tag{2.22}$$

and thus we get the total TKE as

$$k_{tot} = k_{res} + k_{sgs} = \frac{1}{2} \langle \bar{u_i}'' \rangle^2 + \langle k_{sgs} \rangle. \tag{2.23}$$

Previously mentioned, the resolution of the mesh for implicit LES is important as the filter width should reflect the remaining unresolved eddies. Looking at the energy spectrum in wave number space for different turbulence methods in Figure 2.2, we can see that for LES to accurately capture the flow field, the amount of modelled TKE (k_{sgs}), which is the area marked with "LES", should be kept in the dissipation range to ensure that the model is not overly diffusive.

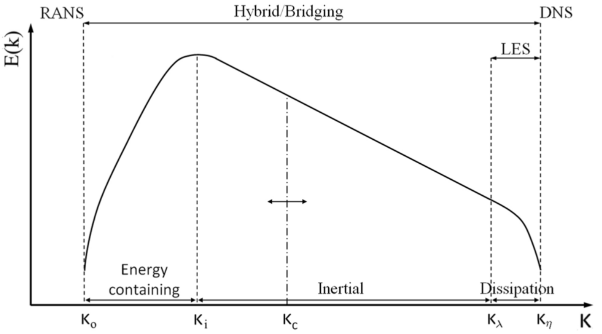

Figure 2.2: Energy spectrum in wavenumber space for RANS, LES and DNS [34]. The TKE is calculated by the integral of the curve, such that the area under the curve represents the amount calculated.

2.3 Dimensionless numbers

The shear Reynolds number

In wall-bounded flows, such as pipes and channels, the viscous stress close to the wall is dominant and is important to model accurately [23]. The most common parameter used to describe its effect on the flow, and as a global parameter for comparison in literature, is the shear Reynolds number

$$Re_\tau = \frac{u_\tau \delta}{\nu}. \tag{2.24}$$

Here $u_\tau = \sqrt{\frac{\tau_w}{\rho}}$, where τ_w is the wall shear stress, is the shear velocity and δ is the length scale, i.e. $\delta = R$ for a pipe. As the viscous length scale is $\delta_v = \nu/u_\tau$ [23], the shear Reynolds number describes the ratio of the lengthscale to that of the viscous lengthscale.

The Dean number

The Dean number is a dimensionless number used to describe the secondary flow in helical and curved pipes [3] which induces vortices called Dean vortices

$$De = Re\sqrt{\frac{D}{2R_c}}. \tag{2.25}$$

Here Re is the Reynolds number, D is the diameter of the pipe and R_c is the radius of the coil.

2.4 Numerical implementation

The Finite Volume Method in OpenFOAM

FVM is a way to discretize partial differential equations by splitting up the computational domain into small control volumes and integrating over them to get equations for the fluxes into and out of the control volume using Gauss divergence theorem, which states that the a volume integral of the divergence of a vector is equal to the sum of the fluxes on the volume [13]. From [35], when this method is applied to Equation (2.1) and Equation (2.2), we get the semi-discretized momentum equation

$$\int_t^{t+\Delta t} \left[\left(\frac{\partial u_i}{\partial t} \right)_P V_P + \sum_f \vec{S} \cdot (\vec{u} u_i)_f + (\nabla p)_P V_P - \sum_f \nu_f \vec{S} \cdot (\nabla u_i)_f \right] dt \\ = \int_t^{t+\Delta t} (S_u V_P + S_p V_P u_{iP}) dt, \quad (2.26)$$

and the discretized continuity equation

$$\sum_f \vec{S} \cdot (\vec{u} u_i)_f = 0, \quad (2.27)$$

where u_i is the transported velocity, V_P is the volume of the current cell P, $\vec{S}$ is the face-area vector, and the right hand side of the equation is the source-terms. Equation (2.26) is "semi-discretized" due to the first term being a temporal derivative. It can be discretized by using a second order scheme the Backward Differencing in time u such as the implicit second order accurate backward scheme[35]

$$\frac{\partial u_i}{\partial t} = \frac{\frac{3}{2} u_i^n - 2u_i^{n-1} + \frac{1}{2} u_i^{n-2}}{\Delta t} \quad (2.28)$$

Here the index n represents the timestep. All transported quantities (exemplified by u_i in Equation (2.26)), can be spatially discretized by using different numerical schemes such as the conservative second order central differencing scheme

$$u_w = u_W + (x_w - x_W) \frac{u_P - u_W}{(x_P - x_W)}. \quad (2.29)$$

Capital letters represents a cell-center while lower case represents a cell-face in an one dimensional mesh, as depicted in Figure 2.3.

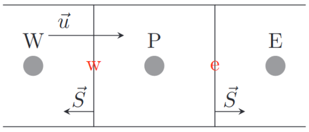

Figure 2.3: Diagram of a one dimensional mesh.

To solve the system of equations from Equation (2.26) through Equation (2.29), the Pressure implicit with splitting of operator (PISO) [36] algorithm can be used. The linear systems to be solved is set up by first defining Equation (2.26) as a set of algebraic equations $M[\vec{u}]$ [37] using the discretization schemes such that

$$M[\vec{u}] = -\nabla p \tag{2.30}$$

here

$$M[\vec{u}] = A\vec{u} - \mathbf{H}, \tag{2.31}$$

where A and $\mathbf{H}$ is the diagonal and off-diagonal contributions of $M[\vec{u}]$ respectively. This gives the momentum correction equation

$$\vec{u} = \frac{\mathbf{H}}{A} - \frac{1}{A}\nabla p. \tag{2.32}$$

The volumetric flux (ϕ) corrector equation is given by

$$\phi = \left(\frac{\mathbf{H}}{A}\right)_f \cdot \vec{S} - \left(\frac{1}{A}\right)_f \vec{S} \cdot \nabla p_f. \tag{2.33}$$

Substituting Equation (2.33) into Equation (2.27) we get the pressure equation

$$\nabla \cdot \left[\left(\frac{1}{A}\right)_f \nabla p\right] = \nabla \cdot \left(\frac{\mathbf{H}}{A}\right)_f. \tag{2.34}$$

In OpenFOAM, PISO [36] is implemented as follows;

1. Initial values of u_i, p and ϕ
2. Start of timestep
3. Apply boundary conditions
4. Solve the momentum equation in Equation (2.30)
5. Build A and $\mathbf{H}$ with the new $\vec{u}$
6. Solve the equation for the volumetric flux Equation (2.33)
7. Solve the pressure equation Equation (2.34)
8. Repeat steps 6 and 7 for the prescribed number of non-orthogonal correction loops
9. Calculate a final momentum correction equation Equation (2.32)
10. Repeat from step 5 for the prescribed number of corrector loops
11. Advance timestep

2.5 Wall-treatment in large eddy simulation

The concept of LES can be split up into many sub-categories, of which the three overarching ones according to Pope [23], are LES with near-wall resolution (WRLES), LES with near-wall modelling (WMLES), and very-large-LES. The two former are the focus in this thesis. In WRLES the whole grid is fine enough to resolve 80% of the energy spectrum, leading to regions of refinement towards the wall in the inner layer Figure 2.4 where there is more turbulent kinetic energy. On the other hand, in WMLES the grid resolution is fine enough to resolve 80% of the energy spectrum away from the wall such that refinement regions towards the wall are replaced by wall-models.

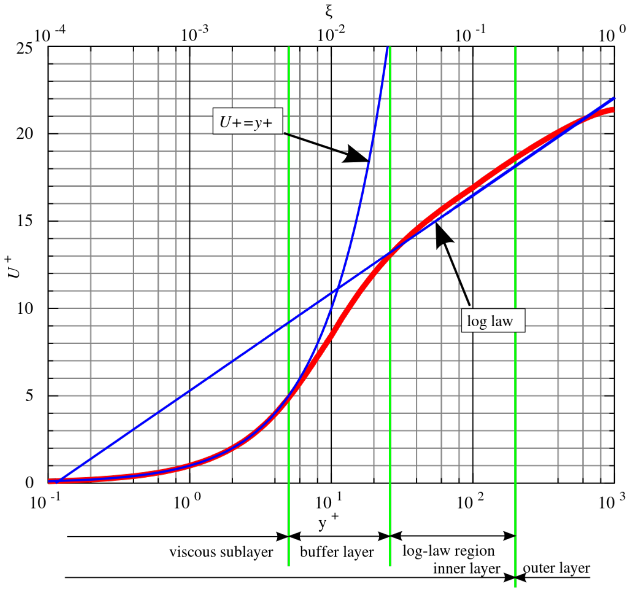

Figure 2.4: Plot of a turbulent boundary layer plotted with Law of the wall[38].

In industrial applications with moderate to high Reynolds number WRLES is less feasible as the viscous length scale δ_v decreases with the the increase of the Reynolds number as $\delta_v/\delta = Re^{-0.88}$ where δ is the length scale of the flow [23]. Chapman [39] estimated that the required grid resolution in the near-wall region increases as $Re^{1.76}$ for WRLES since it scales with δ_v. Newer findings suggests that this increase is higher such that the resolution scales as $Re^{17/9}$ [40]. WMLES on the other hand scales only with δ which again scales with the grid spacing and filter width, making it independent of the Reynolds number [23].

In LES, particularly using FVM, the requirement of a hexahedral grid with somewhat uniform wall-units spacing increases the necessary cell count when using an O-grid mesh. Wall-units, namely x^+, y^+ and z^+, are a measure of distance in viscous length scales as seen in Equation (2.38). To get around these requirements, wall-modelling can be used. WMLES has much less strict requirements for the geometry as it does not require a large amount of cells in the boundary layer [23], which is beneficial for geometries enclosed in walls. Cells can, and should, also be kept as isotropic is possible throughout the boundary layer. This reduces the cell count such that a much more coarse grid can be used compared to DNS. In this thesis we are going to investigate the difference in accuracy and cell count, between WMLES and WRLES in OpenFOAM.

Wall-modelling

The creation of a single function used to represent the velocity profile in turbulent boundary layers is a widely researched field [41]. It is based on dimensional analysis of the flow field near a smooth impermeable surface which gives

$$\frac{\langle u_z \rangle}{u_\tau} = f\left(\frac{u_\tau y}{\nu}\right), \tag{2.35}$$

and consequently

$$-\frac{\langle u_z u_y \rangle}{u_\tau^2} = g\left(\frac{u_\tau y}{\nu}\right). \tag{2.36}$$

Here $\langle u_z \rangle$ is the time-averaged velocity of a stable turbulent flow in the z-direction such that

$$\langle u_z \rangle = \frac{u_z^{k+1} - u_z^k}{\Delta t}, \tag{2.37}$$

where k is the timestep index, and Δt is the length of the timestep. $u_\tau y/\nu$ can be represented as y^+ and $\langle u_z \rangle/u_\tau$ as u^+. This relation is valid for the inner-layer in Figure 2.4. Due to the Reynolds stresses being negligible close to the surface, for $y^+ < 3$ according to Bradshaw and Huang [41] although Spalding [42] gives a more comprehensive summary of the various validity ranges found in the literature, integration of the viscous stress law $\tau = \mu \frac{d\langle u_z \rangle}{dy}$ gives $\langle u_z \rangle = \tau_w y/\mu$, leading Equation (2.35) to take the linear form

$$\langle u_z \rangle^+ = y^+. \tag{2.38}$$

Differentiating and subsequently integration of Equation (2.35) gives the well known logarithmic law of the wall, depicted as "log law" in Figure 2.4.

$$\langle u_z \rangle^+ = \frac{1}{\kappa} ln\left(y^+\right) + C. \tag{2.39}$$

Here κ is the von Kármán constant, and C is a constant. However, Equation (2.39) poses problems for no-slip walls as it is undefined for $y^+ = 0$, as well as giving a non-zero profile at the boundary layer as seen in Figure 2.4 where the unmarked blue line represents the profile of a laminar boundary layer. To improve on Equation (2.39), Spalding [42] presented a single equation for the velocity profile as

$$y^+ = \langle u_z \rangle^+ + e^{-\kappa B}\left[e^{\kappa \langle u_z \rangle^+} - 1 - \kappa \langle u_z \rangle^+ - \frac{1}{2}(\kappa \langle u_z \rangle^+)^2 - \frac{1}{6}(\kappa \langle u_z \rangle^+)^3\right]. \tag{2.40}$$

Here B is a constant. This equation has been showed to give more accurate results for pipe- and flat-plate flow [43]. Therefore, the chosen wall model in this thesis is Spalding's algebraic law of the wall.

In OpenFOAM there is no extensive framework for wall-modelling in LES, but due to it being open-source there exists a community made library for OpenFOAM created by Timofey Mukha (https://github.com/timofeymukha/libWallModelledLES) which can be compiled locally and is easy to use. The package consists of multiple wall-modelling methods, as well as good documented results and best practices [32]. In the following section we will explain how the employed wall model works with dominant flow in the z-direction.

The wall-model algorithm works by initially sampling values of the time-averaged filtered velocity $\langle \bar{u}_{zP} \rangle$ and ν_P in the cell-center P in the LES-domain, some wall-normal distance h from the wall-face, as illustrated in Figure 2.5.

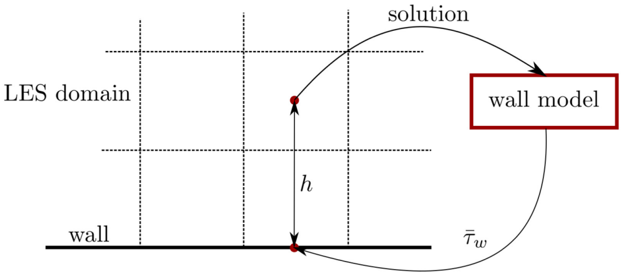

Figure 2.5: Illustration of the wall model implementation from Mukha et. al.[32].

These values are then used in the non-linear algebraic equation Equation (2.40) to obtain values for $\langle \bar{u}_z^+ \rangle$, by using the Newton-Raphson method to find the roots

$$\langle u_z \rangle^+_{n+1} = \langle u_z \rangle^+_n - \frac{y^+(\langle u_z \rangle^+_n)}{y^{+\prime}(\langle u_z \rangle^+_n)}. \tag{2.41}$$

Here n is the iteration index. The wall shear stress $\bar{\tau}_w$ on the adjacent wall face can then be calculated using the relation in the viscous sublayer in Equation (2.38) such that

$$\bar{\tau}_w = \left(\frac{\nu \langle u_z^+ \rangle}{y} \right)^2. \tag{2.42}$$

This value for $\bar{\tau}_w$ is then used to find ν_t on the same wall face with

$$\nu_t = \frac{\bar{\tau}_w}{(\langle \bar{u}_{zP} \rangle / \Delta y)^2} - \nu. \tag{2.43}$$

The wall function is defined as a boundary condition for ν_t on the wall patch, while the sampling point is defined as a wall normal distance in an extra field entry as a scalar h, making it applicable for any geometry.

Wall-resolved

LES without the use of wall-modelling techniques, requires the resolution of the grid in the boundary layer to be fine enough to capture 80% of the TKE from the smaller eddies near the wall such that viscous region is resolved, since the peaks of important quantities like the Reynolds stress anisotropy is within the region $1 < y^+ \leq 20$ [23]. $y^+ \leq 1$ is desired, with a gradual growth rate GR to the outer domain of $1 \leq GR \leq 1.2$. The growth rate is the increase in cell height where for $GR = 1.2$ the height of each cell is 20% higher than the preceding one, as illustrated in Figure 2.6.

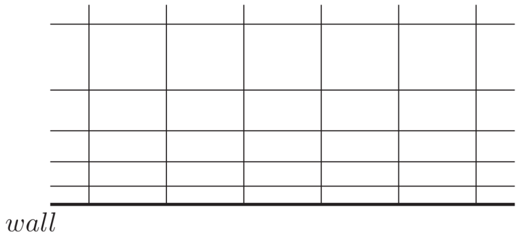

Figure 2.6: Illustration of a resolved boundary layer mesh near the wall showing the increase in cell height.

This poses a problem in circular geometries with a hexahedral mesh, as it increases the aspect ratio of the cell requiring the mesh to be refined to the point where it reaches DNS resolution near the wall, causing a trade off between a high number of cells to keep uniformity and the correct filter size in the transition region. For low Reynolds number flows in particular, the boundary layer stretches further into the geometry, and as such, more attention to the growth of the cell size is required due to the larger range of eddies. On the other hand, for high Reynolds number flows the boundary layer shrinks in height and thus the difference in cell size between the boundary layer and the outer layer increases drastically. Due to the decrease of the viscous length scale, a much higher resolution is required. This in turn requires a smaller timestep for a stable and accurate simulation, due to the requirement that the Courant number

$$Co = u_i \frac{\Delta t}{\Delta x_i} \tag{2.44}$$

should be $Co < 1$ to achieve a stable simulation, and to resolve the time scale for the dissipation of the small scales near the wall. Due to this increased resolution requirement in time and space, WRLES in high Reynolds number flows is still unfeasible for industrial applications due to the high computational cost, as outlined by NASA in "*CFD vision 2030 study: a path to revolutionary computational aerosciences*" [44].

CHAPTER 3

Methods of meshing and simulation

The creation of meshes in CFD can often be the most labour-heavy part of a simulation, but the process is usually omitted from the final thesis and/or paper. There is therefore little research or reasoning behind the different techniques used for meshing pipes. To create a good hexahedral mesh in a circular geometry, the cross-section should be split into different axisymmetric geometries such that manual edge refinement can be applied. In this chapter we will first go through some central meshing parameters, then the meshing techniques and meshes used for simulating periodic turbulent flow in a pipe, before lastly going through the meshes and geometrical parameters for turbulent flow in a helically coiled pipe. The simulation setup will be explained at the end of each respective geometry section.

3.1 Mesh-quality parameters

When creating the mesh, parameters such as non-orthogonality and skewness should be taken into consideration as to not add too much numerical diffusion or instabilities to the solution [35] [45].

Non-Orthogonality

The non-orthogonality NO of a mesh is a measurement of how much the angle of the face-normal vector $\vec{S}$ deviates from the cell-center to cell-center vector $\vec{\Delta}$. Here P is the current cell-center, E is the adjacent cell-center, f is the center of the face between the two cells, and $\vec{k}$ is the deviation vector between $\vec{S}$ and $\vec{\Delta}$.

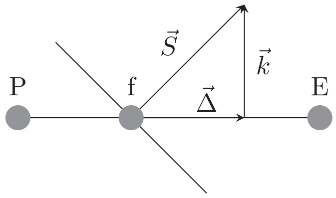

Figure 3.1: Diagram of the face-area vector.

Non-orthogonality is calculated by

$$NO = cos^{-1}\left(\frac{\vec{\Delta} \cdot \vec{S}}{|\vec{\Delta}||\vec{S}|}\right). \tag{3.1}$$

Having a high non-orthogonality when using hexahedral cells ($NO > 30°$) in LES simulations is undesirable, as it increases the number of non-orthogonal correction loops needed in solution algorithms for explicit calculation of $\vec{k}$ to counteract the loss of accuracy and added numerical diffusion when calculating the velocity gradient in the diffusion term in Equation (2.26) [13]. In an O-grid type mesh, it is necessary to sacrifice orthogonal quality in some areas of the mesh to ensure a smooth transition from the outer to the inner region. This does not pose too much of a problem if the average non-orthogonality is kept sufficiently low ($NO < 20°$).

Skewness

The skewness SN of a mesh is the deviation vector between the center point on a cellface and point on the face where the distance vector between the cell centers intersects the face.

$$SN = \frac{\vec{Pf} - \frac{\vec{S} \cdot \vec{Pf}}{\vec{S} \cdot \vec{PE}} * \vec{PE}}{|\vec{Pf} - \frac{\vec{S} \cdot \vec{Pf}}{\vec{S} \cdot \vec{PE}} * \vec{PE}|}, \tag{3.2}$$

using Figure 3.1 as reference, $\vec{Pf}$ is the vector between the the current cell center and the center of the face of the adjacent cell and $\vec{PE}$ is the vector between cell centers P and E. Due to the fact that the calculated quantity varies at best linearly between cells when using FVM [46], and is taken as the average value in the center node of the face, a mesh with high skewness ($SN > 1$) would add too much numerical diffusion for the solution too be accurate. As seen in both Equation (3.2) and Equation (3.1), the numerical diffusion added by meshing errors disappears as the cells approach perfect rectangular cuboids [35] [46].

Resolution

The resolution requirement of the mesh in LES is in-between the required resolution for a RANS and DNS, as mentioned in Section 2.2. As the goal of the LES is to resolve at least 80% of the energy spectrum, a parameter for estimating the quality of the mesh is by the ratio of the resolved turbulent kinetic energy k_{res} to the total turbulent kinetic energy k_{tot}. This can be calculated as a scalar field η by

$$\eta = \frac{k_{res}}{k_{tot}}. \tag{3.3}$$

3.2 Creation of mesh geometry for pipes

Meshing strategies

We used three different mesh strategies to compare the accuracy and applicability for LES simulations. One classic O-grid mesh depicted in Figure 3.2a, one bell-curve type depicted in Figure 3.2b which was automatically created with a commercial software without dividing the geometry, and finally, we propose a new type of pipe mesh rarely seen in FVM literature depicted in Figure 3.2c with a resolved boundary layer and without a resolved boundary layer depicted in Figure 3.2d.

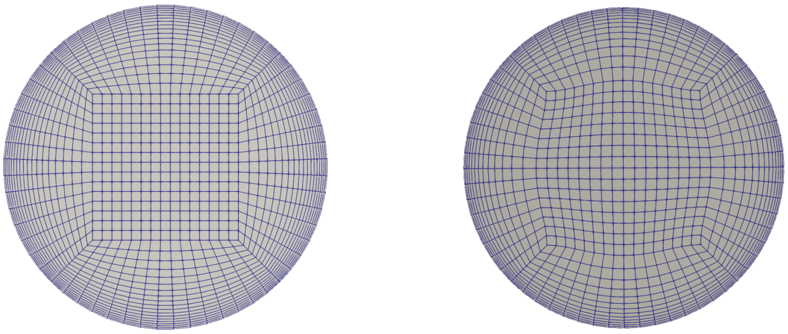

(a) Classic O-Grid (b) Bell-curve O-grid

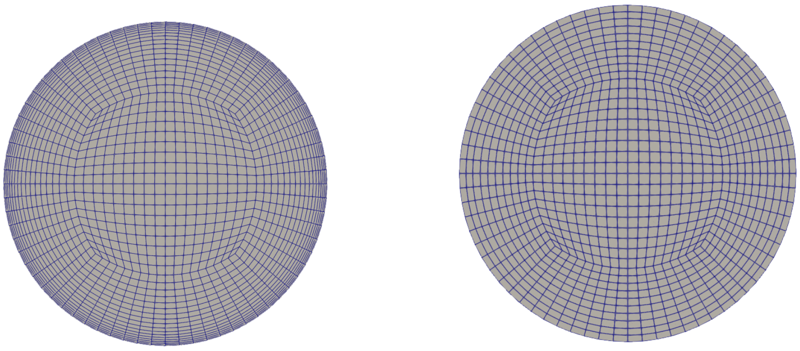

(c) Wall-resolved mesh (d) wall-modelled mesh

Figure 3.2: Cross sectional view of 4 different mesh types. (a) shows a classic O-grid mesh, (b) shows a automatically generated bell-curve O-grid, and (c) and (d) show the new meshes created with resolved and unresolved boundary layer respectively.

To create the new meshes we split the geometry into five parts. The boundary layer was split into four regions, while the core region was created by four arcs with their center outside of the core region as depicted in Figure 3.3. By adjusting the radius of each of the arcs r_i, the core can be adjusted to give a more cubic shape if needed. This depends on the refinement parameter N_a. The most notable difference between this mesh and the other meshes in Figure 3.2, is that the corners of the inner regions cause minimal distortion of the boundary layer, which for low Reynolds numbers spans almost the entire radius of the pipe.

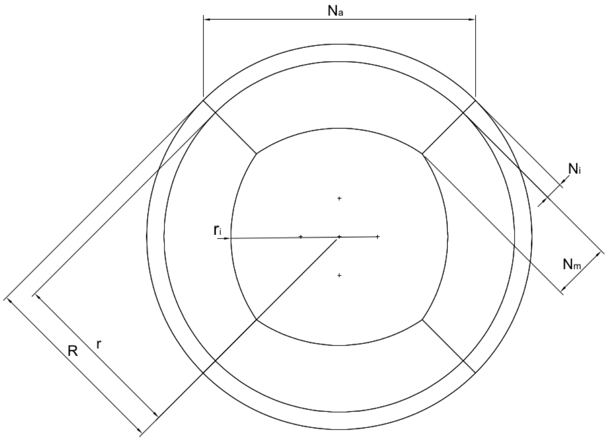

Figure 3.3: Schematic of the extruded profile for the new mesh. Here N_a is the number of the divisions in the azimuthal direction and N_i and N_m is the number of divisions between the turbulent boundary layer and the middle of the pipe. R is the radius of the pipe, while r is the radius to the refinement region near the wall.

Meshes used for validation

We settled on four different meshes to use for comparing against the DNS data from Yamamoto [11] and El Khoury et. al. [19]. We created two meshes for wall-modelling and two for wall-resolved simulations with two refinement levels for each as depicted in Figure 3.4. The data for these meshes are shown in Table 3.1. The nomenclature used for the four different meshes will be represented by an abbreviation of the technique used, WM for WMLES and WR for WRLES, and a final character will be added to represent the level of refinement, C and F for coarse and fine respectively. WM-C denotes the coarsest mesh used with wall models and is depicted in Figure 3.4a, WM-F denotes a mesh with a higher resolution used with wall models, depicted in Figure 3.4b. WR-C denotes the coarsest mesh used with a resolved boundary layer as depicted in Figure 3.4c and WR-F denotes the mesh with the highest resolution used with a resolved boundary layer depicted in Figure 3.4d. WM-C and WR-C feature the same refinement in the azimuthal direction, but they are created for WMLES and WRLES respectively. As seen in Figure 3.4, we found that the core-region of the mesh has to be re-designed based on the resolution of the mesh as the non-orthogonality and skewness in the corners increase drastically with the resolution in the azimuthal direction, i.e. as N_a in Figure 3.3 is increased, if the core-region is not expanded.

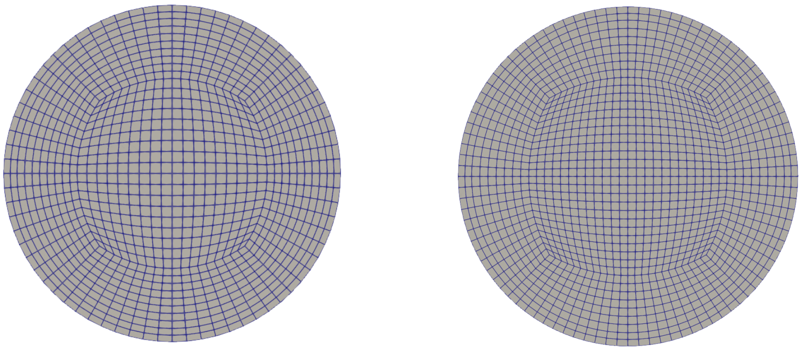

(a) The WM-C mesh (b) The WM-F mesh

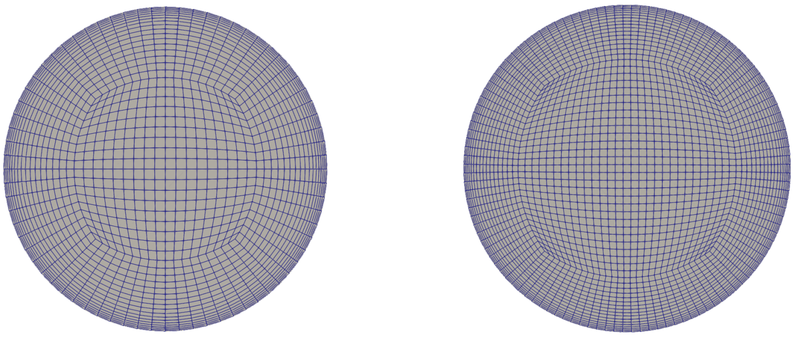

(c) The WR-C mesh (d) The WR-F mesh

Figure 3.4: Cross-sectional view of the meshes used for comparing results from WR- and WMLES to DNS data. (a) and (b) show the two different refinement levels used for WMLES, while (c) and (d) show the two refinement levels used for WRLES.

Case	n_{cells}	NO_{max}	NO_{avg}	SN	y^+
WM-C	93960	56.1	9.2	0.6	10.4
WM-F	172800	51	9.1	0.6	10.8
WR-C	139320	56.1	7.5	0.6	0.6
WR-F	421950	62.9	9.4	0.6	0.6

Table 3.1: Mesh parameters of the meshes used for comparing results from WR- and WMLES to DNS data. n_{cells} denotes the number of hexahedral cells in the mesh, NO_{max} and NO_{avg} the maximum and average non-orthogonality, SN the skewness, and y^+ is the height of the first cell in wall units

3.3 Simulation setup for periodic turbulent flow in a pipe

To develop a fully turbulent flow we performed a perturbation with a laminar flow profile in the z-direction, and waves in the azimuthal direction using a modified perturbation utility for pipes which can be found on github(https://github.com/Jacobhudt/CFD-Tools/tree/master/OpenFOAM/perturbJ/OFv2106). We found that, in agreement with Yamamoto [11], the perturbations were mesh-dependent and as such using interpolation between identical geometries can be beneficial over performing many iterations of perturbations for each mesh to ensure the development of turbulence.

To get fully developed flow in the pipe, we utilized cyclic boundary conditions such that the master-side boundary B is mapped to the slave-side boundary A. Due to the symmetrical features of a pure hexahedral mesh, no interpolation between the patches were needed.

Figure 3.5: Side-view of the schematic for the periodic pipe.

We aimed to reach a fully developed turbulent flow with $Re_\tau = 180$ and $Re_b = 5300$ to compare the results with [19] and [11]. In OpenFOAM, periodic flow is driven with a function called "meanVelocityForce" which applies a pressure gradient force to drive the flow based a user-specified bulk velocity U_{b_0}.

$$\frac{dp}{dz} = \hat{a_p}(|U_{b_0}| - |\hat{U_b}|), \tag{3.4}$$

where a_p is the diagonal coefficient matrix [45] and the hat $\hat{}$ denotes the volume-averaged calculated quantities. The pressure gradient is calculated and updated each timestep. OpenFOAM prints the calculated pressure gradient each timestep, and since we have the relation

$$\frac{dp}{dz} = 2\frac{u_\tau^2}{R}, \tag{3.5}$$

from Yamamoto[11] the convergence of the global flow quantity Re_τ can be monitored during the run as

$$Re_\tau = \frac{R}{\nu}\sqrt{\frac{R}{2}\frac{dp}{dz}}. \tag{3.6}$$

We ran in total eight different simulations of the periodic pipe; six with the WALE turbulence models on the meshes in Figure 3.4, Figure 3.2b and Figure 3.2a, two with the Smagorinsky model on Figure 3.4a and Figure 3.4c. We ran all the simulations using the PISO-algorithm [36] with three inner correction loops and three correction loops for non-orthogonality. The boundary conditions for the pipe are outlined in Table 3.2. The boundary conditions at the wall was set to the no-slip condition (i.e. zero velocity at the boundary face) for the velocity, and zero gradient for the pressure and, ν_t except for the wall modelled cases where the boundary condition was set to Spalding's Law of the wall, explained in Section 2.5.

Variable	**Inlet (A)**	**Outlet (B)**	**Wall**
$\vec{u}$	Cyclic	Cyclic	No-Slip
p	Cyclic	Cyclic	Zero gradient
ν_t	Cyclic	Cyclic	Spalding's Law of the wall / Zero gradient

Table 3.2: Boundary conditions for the periodic pipe. Spalding's Law of the wall was used for the wall-modelled simulations, while zero gradient was used for the wall-resolved simulations.

The numerical schemes used are outlined in Table 3.3. Central difference was used to discretize both the gradient and divergence terms due to it being second order accurate and non-diffusive, while the temporal term was discretized with a second order backward scheme. A full corrector was applied to the laplacian in order to reduced any errors induced by areas with high non-orthogonality.

Term	**Scheme**
temporal	backward
gradient	linear
divergence	linear
laplacian	corrected

Table 3.3: Numerical schemes for the periodic pipe. The temporal term is discretized with a second order backwards differencing scheme, and both the gradient and divergence were discretized by second order linear interpolation i.e. central differencing. The laplacian scheme is corrected using multiple non-orthogonality correction loops.

3.4 Meshing of helically coiled pipes.

To simulate turbulent flow in helically coiled pipes, we swept the cross-section depicted in Figure 3.3 along a helical path according to three of the specifications from Yamamoto [11]. The geometry was made using Autodesk Fusion 360, which has a coil-generator built in, giving the user a good starting point for sweeping of different profiles. We made some design changes at the outlet, as the CAD employed by Yamamoto reportedly were limited in that the outlet could not be extended in the normal direction of the coils cross section. Furthermore, we chose to refrain from using an extended pipe at the beginning of the pipe and we instead incorporated a small jointing area for C1, which facilitated a smooth and controlled transition at the inlet. In the schematic of C3 Figure 3.6, one can see the different geometrical parameters summarized in Table 3.4. The pitch P, which is the distance between the center point of the coiled pipe to the centerpoint in the proceeding revolution, depicted in Figure 3.6, is used with the radius of the coil R_c, which is the distance from the center of the coil to

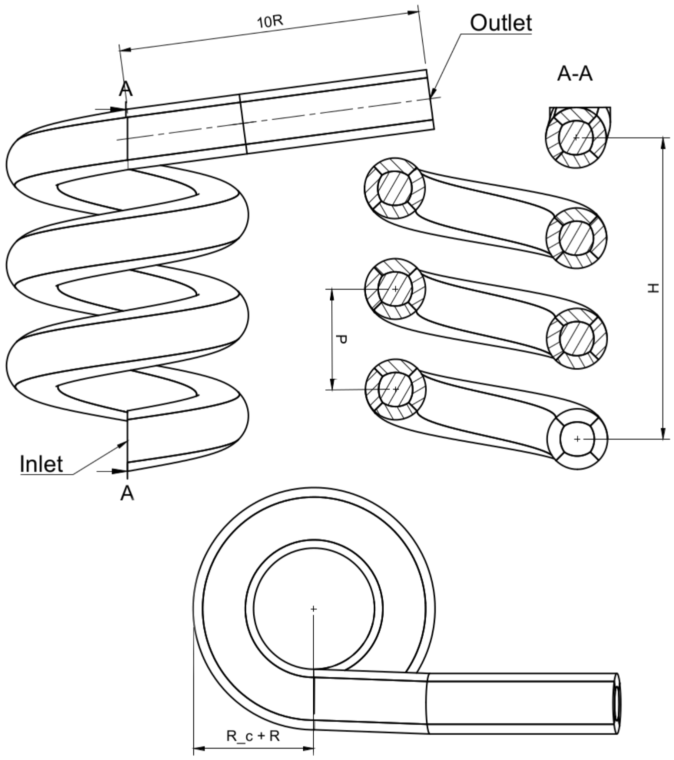

Figure 3.6: Schematic of the longest coil, C3. The top left picture shows a side-view of the coil and the length of the straight outlet section, the top right picture shows a cross-sectional view of the coil with the measurement points for the pitch and the total height. The bottom picture shows a top-view of the coil where the radius of the coil R_c is the distance from the center point of the coil to the center point of the cross-section.

the centerline of the coiled pipe, to calculate both the curvature

$$\kappa = \frac{R_c}{R_c^2 + \frac{P^2}{4\pi^2}}, \tag{3.7}$$

and the torsion

$$\tau = \frac{P}{2\pi(R_c^2 + \frac{P^2}{4\pi^2})}. \tag{3.8}$$

In Table 3.4 R_c, P, κ and τ are nondimensionalized by the radius of the pipe R. The torsion and curvature of a helix were highlighted as important parameters by Yamamoto [11] due to their applicability in Biofluid mechanics as the geometry of cerebral arteries can be classified by similar parameters. These parameters are also used in literature for characterization of helical coils and similar curved geometry.

Case	n_{rev}	R_c	P	κ	τ	n_{cells}
C1	1	3	10	0.260	0.191	346 608
C2	2	3	5	0.311	0.105	550 188
C3	3	3	3.33	0.323	0.0572	744 372

Table 3.4: Geometrical data for the helical coils normalized with the radius of the pipe R. n_{rev} is the number of revolutions of the coil, R_c is the radius of the coil, P is the pitch, κ is the curvature, τ is the torsion and n_{cells} is the number of cells.

The construction of the three meshes used in this study followed a systematic approach involving face-matching the inlet to the outlet and subsequently performing a sweeping operation across the entire computational domain using hexahedral cells. This mesh generation technique aimed to ensure geometric conformity and consistency throughout the domain. The resulting meshes, depicted in Figure 3.7, exhibit distinct characteristics that are crucial for capturing the intricate flow phenomena within helically coiled pipes using LES turbulence models with a FVM code. The face-matching facilitated the creation of well-matched inlet and outlet boundaries as well as a consistent cross-section in line with Figure 3.6, enabling a smooth and continuous flow transition throughout the computational domain based on the results from the mesh study in Section 3.2. The subsequent sweeping operation, performed using hexahedral cells, facilitated the creation of structured meshes with regular cell shapes.

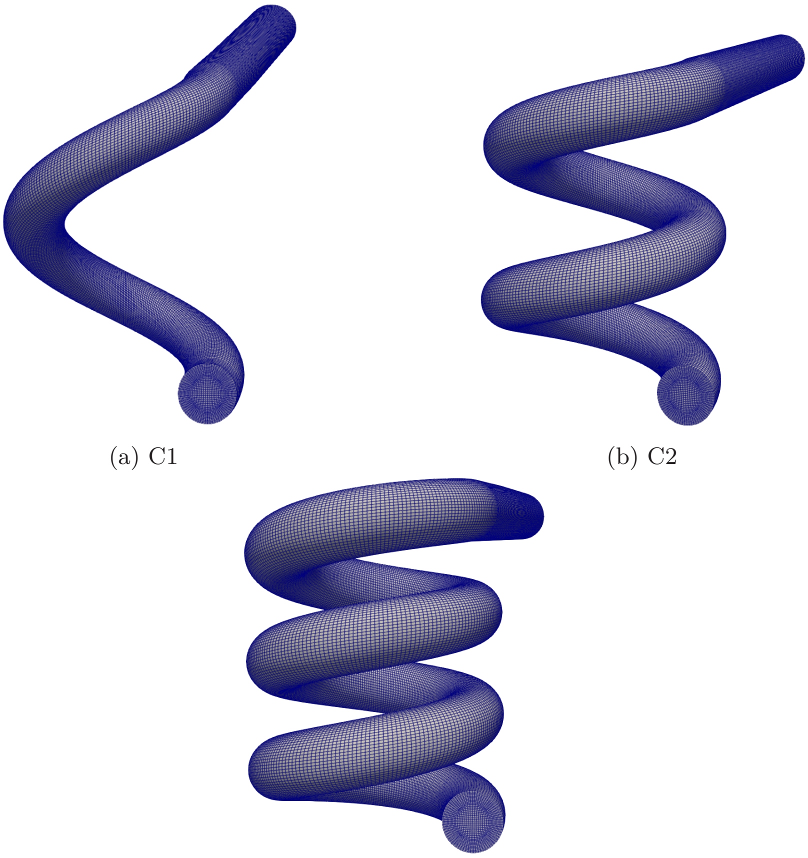

(a) C1

(b) C2

(c) C3

Figure 3.7: The three helical coil geometries used in the simulations.

3.5 Simulation setup for the helically coiled pipes

The simulation setup consisted of mapping the velocity and other relevant flow data obtained from the inlet section of the WM-C mesh, as illustrated in Figure 3.5, once a fully developed flow state was achieved. At each time step, the data was sampled, leveraging the equal-faced configuration of the meshes, thus obviating the need for interpolation between the two faces. In OpenFOAM, this particular type of boundary condition, wherein sampled data is mapped or interpolated to the boundary at each time step, is defined as the boundary condition "timeVaryingMappedFixedValue". The pressure at the outlet was set to zero. All boundary conditions are summarized in Table 3.5. To accurately account for the flow characteristics near the walls, wall models were employed based on the insights obtained from the pipe simulations in Section 3.2. This enhanced the computational efficiency and alleviated the computational burden associated with resolving the near-wall boundary layer which would have drastically increased the cell count. The simulations were run with the PISO-algorithm [36] using three corrector loops and three non-orthogonality corrector loops.

Variable	**Inlet**	**Outlet**	**Wall**
$\vec{u}$	Mapped value	Zero gradient	No-Slip
p	Zero gradient	Fixed value: 0 Pa	Zero gradient
ν_t	Mapped value	Zero gradient	Spalding's Law of the wall

Table 3.5: Boundary conditions for the three coil configurations. Spalding's Law of the wall was used for wall, the pressure at the outlet was set to zero, and the sampled data from the WM-C mesh was used as the Inlet condition.

The numerical schemes used for the three coils are outlined in Table 3.3. The pipe and the coils were discretized with the same numerical schemes, with central differencing for the gradient and divergence terms, second order backward for the temporal term and a fully corrected scheme for the laplacian term.

Term	**Scheme**
temporal	backward
gradient	linear
divergence	linear
laplacian	corrected

Table 3.6: Numerical schemes for the three coils. The temporal term is discretized with a second order backwards differencing scheme, and both the gradient and divergence were discretized by second order linear interpolation i.e. central differencing. The laplacian scheme is corrected using multiple non-orthogonality correction loops.

CHAPTER 4

Results and discussion

In this chapter we will go through the results in three different sections. Firstly, we will present and discuss the results from the mesh study performed, and which features affect the solution, by examining the time-averaged wall shear stress. Secondly we will look at the results from the simulations of the four different cases summarized in Section 3.2. Here, we will see the effect using the WALE or Smagorinsky model has on the solution, how the wall modelled and resolved meshes compares to the DNS data, and how well they resolve turbulent structures along the wall. Lastly, we will examine the result from the simulation done on the three different helically coiled pipes. How the velocity field and pressure distribution differs to that of a straight pipe, the effect the induced spanwise pressure gradient has on the flow, how the turbulent kinetic energy is affected in a helical coil and how it correlates with the torsion and curvature, as well as the appearance of Dean vortices in both the mean and the instantaneous flow.

4.1 Impact of mesh strategy on the solution

In this section, our primary focus will be on the examination of mesh-induced errors and the profound influence of mesh strategy on the numerical solution. Particular attention will be directed towards the bell-type mesh illustrated in Figure 3.2b, and the WM-C mesh depicted in Figure 3.4a. By examining the temporal mean of the results, we seek to gain comprehensive insights into the inherent challenges and advantages associated with each configuration, thereby shedding light on the impact of mesh selection on the accuracy and robustness of the computational results when using FVM for LES.

Streaks in the wall shear stress

The limitations and discrepancies in various meshing techniques for low Reynolds number flows become particularly apparent on the estimation of wall shear stress. This disparity is particularly noticeable when comparing the outcomes obtained from the bell-curve type mesh, which is generated automatically by a commercial meshing software, against those from the WM-C mesh, due to the difference in uniformity in the boundary layer. It should be noted that the reported wall shear stress is in effect divided by the density and thus has the units m^2/s^2.

In Figure 4.1a, distinct streaks can be observed in the distribution of the time-averaged wall shear-stress, exhibiting a clear adherence to the geometric features of the mesh. Thin streaks align with the corners of the inner cuboid, while wider streaks align with the sides of the cuboid. Conversely, Figure 4.2 displays a wall shear stress pattern that lacks any discernible adherence to the geometrical aspects of the mesh. It is noteworthy that similar streaks are not observed in the conventional O-grid, which can be found in Appendix A.

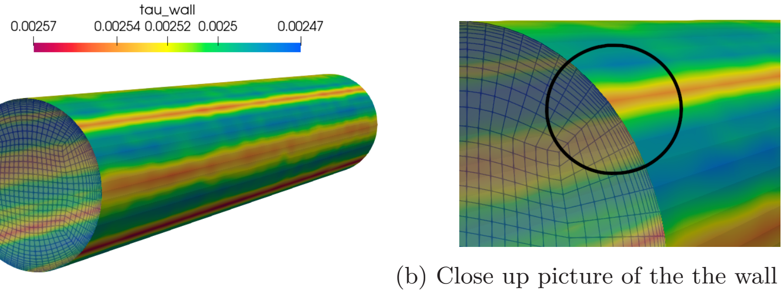

(a) Streaks in the time-averaged wall shear stress in the bell-curve pipe mesh.

(b) Close up picture of the the wall shear stress in the bell-curve mesh illustrating the geometric specific pattern.

Figure 4.1: Streaks in the time-averaged wall shear stress in the bell-curve mesh. (a) shows that the streaks in the whole domain, while (b) shows a close-up of the streaks which aling with the corner of the inner cuboid.

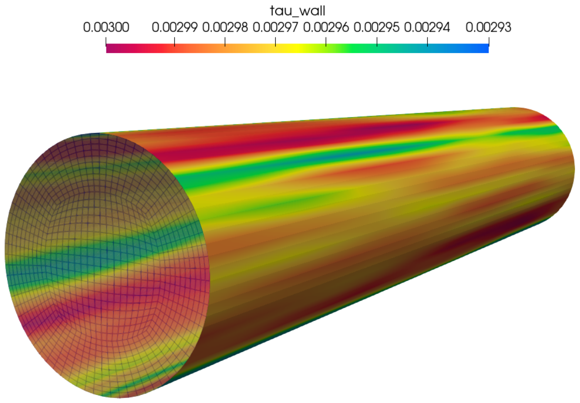

Figure 4.2: Streaks in the time-averaged wall shear stress in the WM-C mesh. The streaks have a randomly distributed pattern of streaks of the wall shear stress.

Looking at the mean values of the time-averaged wall shear stress in Table 4.1, where the analytical value is calculated from a shear Reynolds number of $Re_\tau = 180$, we see that the bell-curve shows better performance than that of the O-grid which has the highest error over all. Both WR-C and WM-C showed improved performance over the two aforementioned meshes.

Case	τ_w $[m^2/s^2]$	**Error**[%]
Analytic	0.002916	–
Bell-curve	0.002506	14.05
O-grid	0.002349	19.44
WR-C	0.002535	13.04
WM-C	0.002974	2.05

Table 4.1: The domain-averaged values of the time-averaged wall shear stress in five different meshes. The analytical value is calculated from the target shear Reynolds number $Re_\tau = 180$, with the error reported in absolute percentage. The bell-curve shows a more accurate prediction when looking at the mean value than the O-grid, which hides the local inaccuracies in the bell-curve from the visual representation.

The uneven distribution of the turbulent kinetic energy

To further emphasize the impact of the chosen mesh strategy we will briefly look at the distribution of time-averaged TKE in all four meshes to see the impact of non-uniform cells in the boundary layer. The TKE was sampled along the red and yellow line depicted in Figure 4.3.

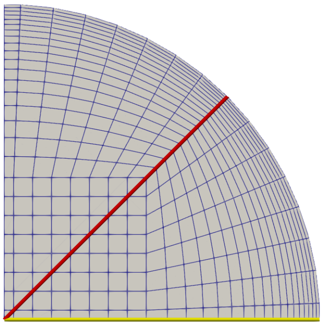

Figure 4.3: Lines used for sampling the TKE in bell-curve, O-grid, WR-C and WM-C meshes.

Presented in Figure 4.4, we see that the TKE in the bell-curve and O-grid is impacted by the deformed boundary layer, hinted to by the results from the wall shear stress, while WM-C and WR-C are impacted to a much less extent. The TKE in the bell-curve, depicted in Figure 4.4a, and the O-grid, depicted in Figure 4.4b, are underestimated in the area of the mesh stretching from the corner of the inner cuboid, while WM-C and WR-C show an even distribution of TKE.

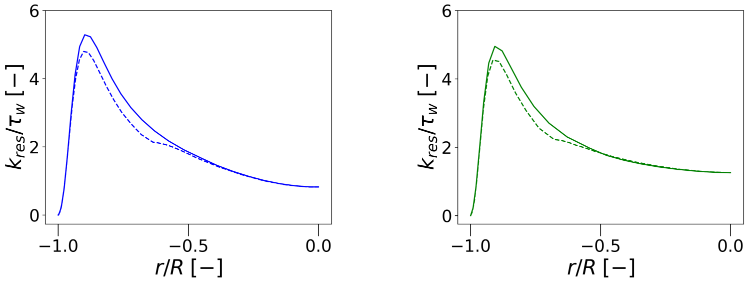

(a) TKE in the O-grid mesh (b) TKE in the bell-curve mesh

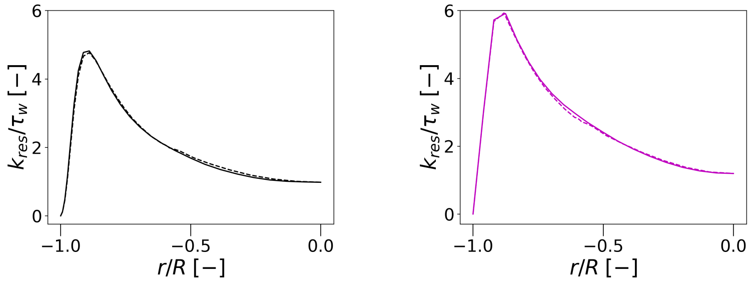

(c) TKE in the WR-C mesh (d) TKE in the WM-C mesh

Figure 4.4: Sampled TKE in the four different meshes. The dashed line (**- -**) is the sampled TKE from the wall to center of the pipe through the corner of the central cuboid, while the filled line (**-**) shows the the TKE sampled along a line from the wall to the center of the pipe through the middle of a side of the central cuboid. Both the bell-curve (a) and the O-grid (b) show reduced TKE due to the non-uniformity of the boundary layer.

Skewness and non-orthogonality

Upon further inspection of the skewness and non-orthogonality, we gain further insight into which of the mesh-quality parameters effected the solution. Looking at the skewness value of the meshes in a cross-section of the pipe in Figure 4.5, shows that the region of high skewness in the bell-curve mesh, depicted in Figure 4.5a, is located in streaks which follow the corner of the inner cuboid towards the wall. The skewness in the WM-C mesh, depicted in Figure 4.5b, shows high values at the cells in the corners of the inner cuboid, while streaks of low skewness extends from the corners towards the wall. Lastly, the skewness in the O-grid, depicted in Figure 4.5c, shows similar behavior to that of the WM-C mesh, where there are regions of high skewness at the corners of the inner cuboid, with streaks with low skewness stretching towards the wall.

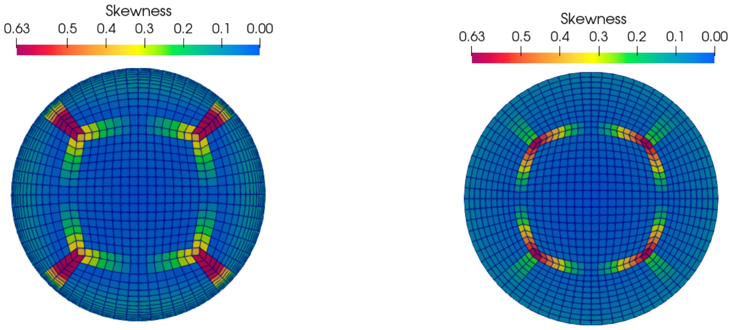

(a) Skewness in the bell-curve type mesh. (b) Skewness in the WM-C mesh.

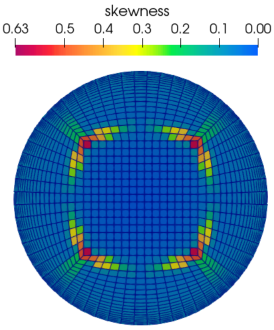

(c) Skewness in the O-grid mesh.

Figure 4.5: Skewness in three different meshes scaled by the same range. (a) shows the increased skewness in the bell-curve mesh extending from the inner cuboid, (b) and (c) show the reduced skewness in WM-C mesh classic O-grid mesh respectively.

The values of the non-orthogonality in the bell-curve, WM-C and O-grid mesh is depicted in Figure 3.1, in a cross-section of the pipe. The bell-curve shows overall to exhibited low values for the non-orthogonality although cells with higher non-orthogonality are located outside the corners of the inner cuboid which extends towards the wall. In the WM-C mesh, depicted in Figure 4.6b, we see high values of non-orthogonality within the corners of the inner cuboid, extending towards the center of the pipe. A similar pattern can be observed in the non-orthogonality of the O-grid, where there is high non-orthogonality in the corners of the inner cuboid which extend towards the center of the pipe.

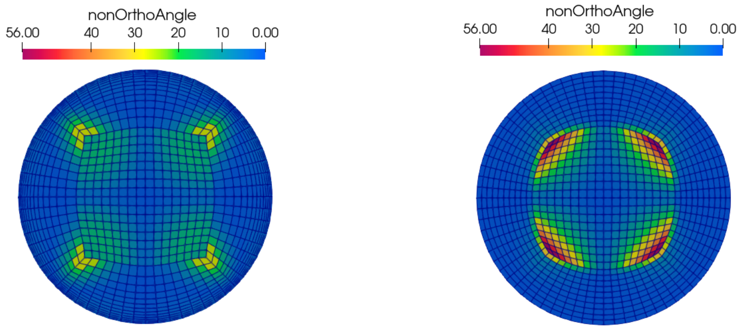

(a) Non-orthogonality in the bell mesh. (b) Non-orthogonality in the WM-C mesh.

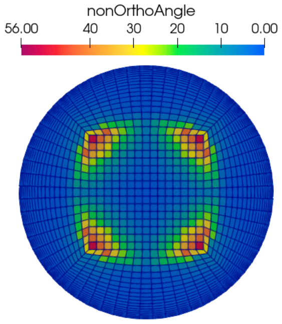

(c) Non-orthogonality in the O-grid mesh.

Figure 4.6: Non-orthogonality in three different meshes scaled by the same range. (a) shows that the overall non-orthogonality is lower than in the proceeding configurations, while it has higher non-orthogonality in the boundary layer. (b) and (c) show that the non-orthogonality is reduced in the boundary layer while it is far greater in the inner cuboid compared to (a).

Discussion of the impact of mesh geometry on the solution

Comparing the results from the wall shear stress in Figure 4.1 and Figure 4.2, we saw that the bell-curve exhibited geometric specific streaks in the wall shear stress, while the wall shear stress in both the O-grid (Appendix A) and the WM-C mesh showed a random distribution of the streaks, which aligns with the expected behavior. This phenomenon can be attributed to the low Reynolds number characterizing the flow within the pipe, resulting in an extended boundary layer that spans a considerable portion of the pipe radius. Consequently, achieving uniformity in the boundary layer becomes crucial. Illustrated in Figure 4.4, it appears that bell-curve and O-grid meshes may not offer an optimal geometry for these specific flow conditions, as the TKE was underpredicted in the cells stretching out from the corner of the inner cuboid. Distortion of the boundary was present in both cases, while the uniform boundary layer of WM-C and WR-C shows good agreement between the two sampled regions.

Considering this behavior, it was deemed essential to visually inspect the wall shear stress rather than solely relying on the average values reported by the OpenFOAM at each time step, which were used to monitor the friction Reynolds number Re_τ in Equation (3.6). This approach was adopted due to the imposed pressure gradient enforced by OpenFOAM, as the reported average value, while accurate, has the potential to conceal these unphysical results. This is outlined in Table 4.1, where the bell-curve showed improved performance over the O-grid when looking at the average value of the time-averaged wall shear stress. By visually examining the wall shear stress distribution, a more comprehensive assessment of the simulation accuracy can be attained, providing valuable insights into potential irregularities or inaccuracies in the flow solution even though the mean value implicates better performance.

When further inspecting the skewness and non-orthogonality, as elaborated upon in Section 3.2, it becomes apparent that the streaks observed in Figure 4.1 can be attributed to the high skewness values within the boundary layer. In Figure 4.5a, the region characterized by the highest skewness extends from the corner of the inner cuboid towards the wall, thereby aligning with the streaks evident in the wall shear stress distribution. Conversely, in Figure Figure 4.5b and Figure 4.5c, the most pronounced skewness values are confined to the corners of the inner cuboid, accompanied by streaks of cells exhibiting approximately a three fold reduction in skewness that extend outward towards the wall.

The non-orthogonality shows again that there is a distortion in the cells stretching outwards from the inner cuboid, depicted in Figure 4.6a. However, the non-orthogonality overall is much lower than what it is in the employed mesh in Figure 4.6b and in the O-grid in Figure 4.6c, which could effect the accuracy of the simulation within the inner region in these meshes compared to Figure 4.6a. Nonetheless, the increased non-orthogonality in the boundary layer in the bell-curve mesh compared to the two other meshes may also be a contributing factor to the observed streaks following the geometrical features of the mesh, as the other two do not feature any discernable values of non-orthogonality outside the inner cuboid.

The skewness and non-orthogonality mainly affects the solution in the form of diffusion as elaborated upon in Section 3.2. Numerical diffusion from high non-orthogonality can be reduced by using the extra correction loops available in OpenFOAM for the PISO-algorithm [36] as it only raises as an error in the diffusion term in Equation (2.26) [35]. The error from the skewness on the other hand, affects each of the face integrals [35] as the value of the transported quantity has to be interpolated from the value of the face to the cell centers. Since skewness is a measure of the deviation between the location of the face center and the calculated to position, it has to be corrected using specialized numerical schemes which are sparsely documented and should be instead corrected on a mesh-level.

4.2 Results for periodic turbulent flow in a pipe

In this section, we will analyze the results obtained from the simulations conducted on the pipe geometries outlined in Table 3.1 and visualized in Figure 3.4. The primary objective is to compare the accuracy of the wall treatment at low Reynolds numbers and examine their agreement with the high-fidelity DNS data reported by Yamamoto [11] and El. Khoury et. al. [19]. Additionally, we will conduct a brief comparison of the performance of the widely used Smagorinsky model and the improved WALE model in transitional flow.

Comparison of Smagorinsky and WALE

To quantify the difference in performance of these two models on transitional flow, we ran four simulation; two on WM-C and two on WR-C. As previously mentioned in Section 2.2, the Smagorinsky model has been noted to exhibit over-diffusive tendencies in certain geometrical configurations [30]. Hence, it was of interest to look at how each model handles transitional flow scenarios, particularly during the transition from laminar to turbulent flow using perturbed velocity profiles. In Figure 4.7 the mean and instantaneous velocity profile of the velocity after 350,000 timesteps is depicted. In both simulations ran with Smagorinsky (plotted with the red line) using WR- and WMLES we can see that both the instantaneous and mean velocity profile overlap, exhibiting a parabolic profile, which is a characteristic of laminar flow. The simulations ran with the WALE model (plotted with the black line) on the other hand, show a flat mean velocity profile, and a jagged instantaneous velocity profile which indicates turbulent flow. The figure shows that the Smagorinsky model appears more dissipative than the WALE model.

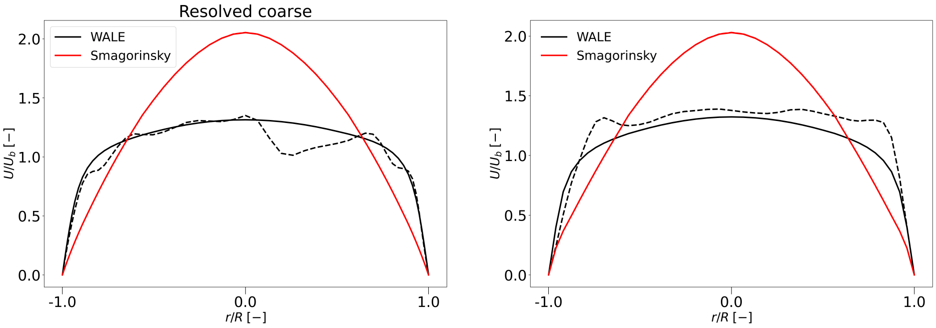

(a) WALE and Smagorinsky in the WR-C mesh.

(b) WALE and Smagorinsky in the WM-C mesh.

Figure 4.7: Velocity profiles of the mean (-) and the instantaneous (- -) colored by black for WALE, and red for Smagorinsky. (a) shows the velocity in the WR-C mesh after 350,000 timesteps, while (b) shows the velocity in the WM-C mesh. In both (a) and (b) the perturbations in the Smagorinsky diffused out, leaving an overlapping laminar profile for the mean and instantaneous velocity.

Global flow quantities

The computed global flow quantities, namely Re_τ and u_τ/U_b, are reported along with their corresponding errors, which are expressed as the absolute percentage deviations from the target values obtained from El Khoury et al. [19].

In Table 4.2 we see that, when using the shear Reynolds number as a metric for examining the performance, the WM-C mesh shows the lowest error and increasing resolution leads to an increase in error, as is evident from the increase in error in WM-F. When the mesh resolution is increased using a resolved boundary layer, there is a subsequent decrease in the error. In the wall-modelled simulations, the target value is overpredicted, while it is underpredicted in the wall-resolved simulations.

Case	$\mathbf{Re}_\tau[-]$	**Error**[%]
El Khoury et. al	180	–
WM-C	181.84	1.02
WM-F	186.13	3.41
WR-C	167.85	6.75
WR-F	174.30	3.17

Table 4.2: Absolute error in percentage in the shear Reynolds number in the four different simulations when compared to the target value from El Khoury et. al. [19]. The simulations with wall models show an overprediction of the target value, while the resolved simulations show an underprediction. WM-C is overall the most accurate using this metric.

Looking at the error in the value obtained for the normalized shear velocity, we see similar behavior to that of the result from the shear Reynolds number. This is due to the fact that the shear Reynolds number is a function of the shear velocity, seen in Equation (2.24). The error increases when the resolution is increased for meshes using wall modelling, and the error decreases with the increase of resolution in meshes using a resolved boundary layer. The WM-C mesh also exhibited the lowest error in this metric.

Case	$u_\tau/\mathbf{U}_b[-]$	**Error**[%]
Khoury et. al	0.0683	–
WM-C	0.0693	1.46
WM-F	0.0709	3.81
WR-C	0.0635	7.03
WR-F	0.0659	3.55

Table 4.3: Absolute error in percentage in the normalized shear velocity in the four different simulations when compared to the target value from El Khoury et. al. [19]. The simulations with wall models show an overprediction of the target value, while the resolved simulations show an underprediction. WM-C is overall the most accurate using this metric.

Mean statistics

This section presents an extensive analysis of mean statistics in the four different cases, comparing the results with those obtained by Yamamoto [11] and El Khoury et. al. [19]. The statistical quantities are plotted in a logarithmic-linear representation, with the wall-normal distance presented in wall units $(1-r)^+$ on the x-axis. The wall-modeled data are depicted using dots and lines to better visualize the coarser resolution in the boundary layer of the wall-modelled simulations compared to the wall-resolved ones. The velocity profiles are normalized to $u_i^+ = u_i/u_\tau$, where $i = z, t, r$, and the Reynolds stress is normalized as $< u_z u_r >^+ = < u_z u_r > /u_\tau^2$. Lastly we will briefly examine the overall mean- and fluctuating velocity profiles.

The normalized mean axial velocity profile in Figure 4.8 shows the difference in the results for the normalized axial velocity in the boundary layer of the pipe. The plot is split into three different regions; The Viscous Sublayer, the Buffer Region and the Log-law region, in accordance with the plot of a turbulent layer in Figure 2.4. The Viscous Sublayer is the region where there is a linear relationship between the quantities such that $u_z^+ = (1-r)^+$. The log-law region is the region where the velocity profile is logarithmic and the buffer region is the overlap region between the two.

Looking at the results for the simulations done with wall models, we see that both levels of refinement deviate from the target data in the buffer region, while WM-C shows an accurate representation in the log-law region, WM-F shows an underprediction in both regions. The two wall-resolved simulations overpredict the result half-way through the buffer region and in the log-law region, but show a good agreement with the target data in the viscous sublayer. The increase in resolution from WR-C to WR-F leads to less overprediction of the result.

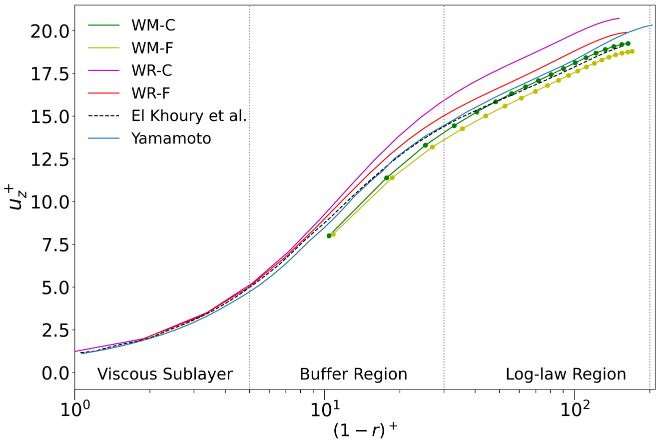

Figure 4.8: The profile of the mean normalized axial velocity four different simulations plotted against the results from El Khoury et. al. [19] and Yamamoto [11]. The horizontal dotted lines represent the three different regions in the turbulent boundary layer. The simulations using wall-models show good agreement with the DNS data in the log-law region, while the resolved simulations overpredict the profile.

In Figure 4.9 we see the profiles of three components of the mean root mean square (RMS) velocity, which is the mean of the fluctuating component of the Reynolds averaged velocity (see Equation (2.21)), and the only non-vanishing Reynolds stress in cylindrical coordinates. In the axial RMS velocity, depicted in Figure 4.9a, we can see that WM-C and WM-F underpredicts the value in the first cell, while the proceeding data shows good agreement with the target data from El Khoury et. al. [19]. WM-F shows a greater underprediction than WM-C at the beginning, while it shows a more accurate result after the two first points. WR-C overpredicts the peak of the velocity with the increase in resolution in WR-F shows an increase in accuracy, being closer to the data from El Khoury et. al. than that of Yamamoto[11].

In the radial RMS velocity, depicted in Figure 4.9c, we see that all four simulations underpredict the target data. For this result WM-F is closer to the target value than WM-C, which is in turn in agreement with Yamamoto [11]. The increased resolution from WR-C to WR-F increases the accuracy, with WR-F being closer to the target value than the other three and Yamamoto [11].

The result for the tangential RMS velocity is shown in Figure 4.9c. Here, WM-F overpredicts the target value at the beginning, while adhering well after the peak. WM-C is accurate in the first few cells, while it underpredicts the peak value of the velocity. Once again, the increased resolution from WR-C to WR-F gives a more accurate result, while its still being underpredicted. Both WM-C, WM-F and WR-F performed better than Yamamoto [11]. For the only non-vanishing Reynolds stress plotted in Figure 4.9d, we see that both the wall modelled simulations perform equally. WR-C underpredicts the data from El Khoury et. al. [19], while WR-F slightly overpredicts it.

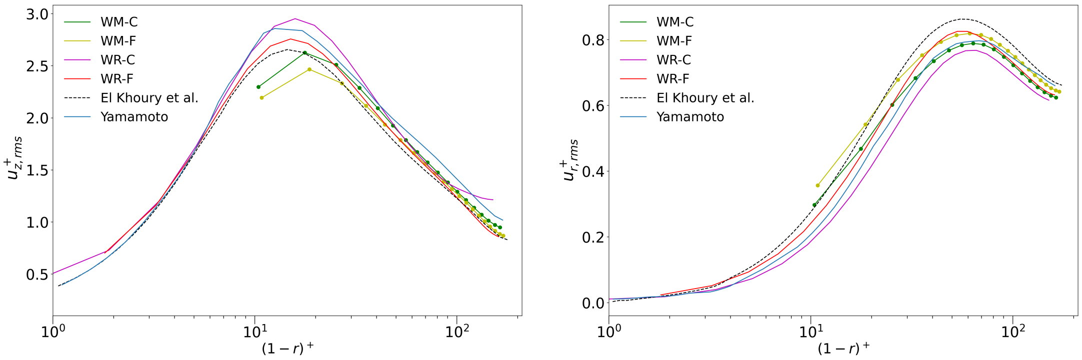

(a) Profile of the axial RMS velocity.

(b) Profile of the radial RMS velocity.

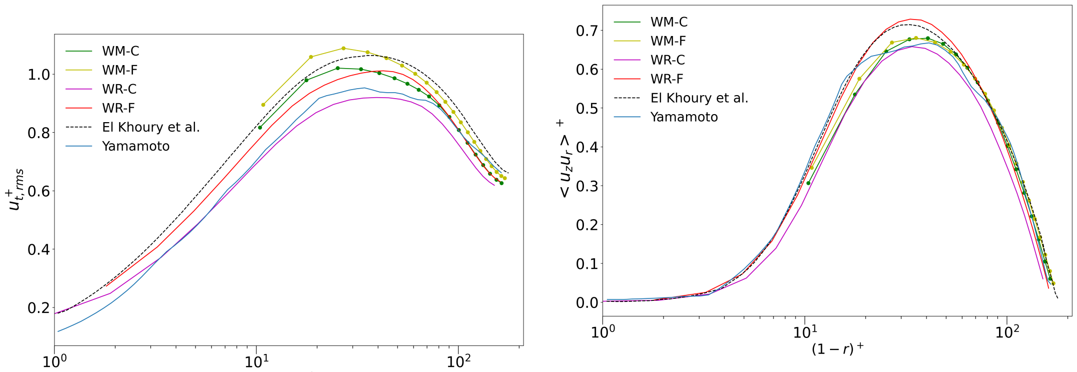

(c) Profile of the tangential RMS velocity.

(d) Profile of the only non-vanishing Reynolds stress.

Figure 4.9: Velocity profiles of the RMS velocities and the non-vanishing Reynolds stress in the four different simulations plotted against the results from El Khoury et. al. [19] and Yamamoto [11]. The simulations done with wall-models show better adherence to the DNS data from El Khoury et. al. [19] than the data from Yamamoto [11] and the WR-C simulation.

The profile of the magnitude of the mean and mean RMS velocity of the pipes is plotted, along with the data from Yamamoto in Figure 4.10, normalized with the bulk velocity of the pipe. The mean velocities in Figure 4.10a shows good agreement to that of Yamamoto [11], with no large deviations from each other. In the plot of the RMS velocity in Figure 4.10b, all four simulations overpredict the values compared to that of Yamamoto [11], with the wall modelled simulations resulting in a more parabolic profile than that of the wall resolved ones.

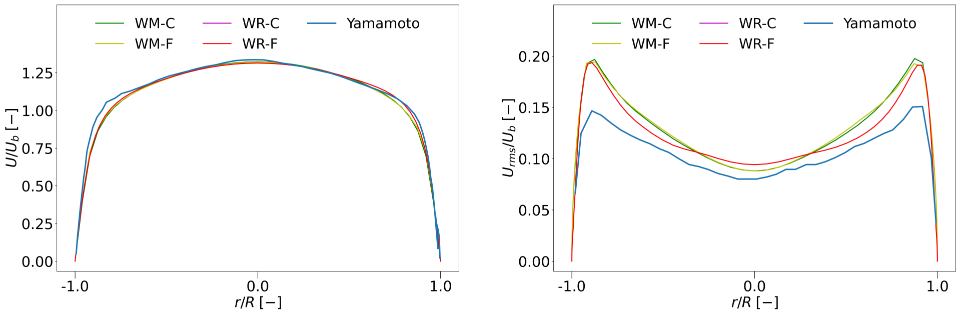

(a) Mean velocity profile. (b) RMS velocity profile

Figure 4.10: Normalized mean velocity profiles of the pipe with the (a) showing the mean velocity and (b) the root-mean square of the velocity. Both quantities are normalized by the bulk velocity and plotted with the data from Yamamoto [11]. The mean velocity profile in (a) shows good agreement to the data from Yamamoto [11], with no discernible differences between the four simulations. The RMS velocity profile shows that the profiles were overpredicted when compared to Yamamoto, and that the simulations using wall models create a more parabolic profile than that of the WR-F mesh.

Turbulent structures near the wall

In CFD, a sufficiently large computational domain, such that all the turbulent structures are captured is crucial. In conventional simulations, i.e. non-periodic on an arbitrary geometry, the inlet and outlet are often extended by a factor of the characteristic length scale. For circular cross-sections this would be the radius R. The extension is usually between $10R$ to $20R$ depending on the problem at hand. This can help with divergence as it helps the flow develop a more fully developed profile before entering and exiting the domain. In periodic geometries where the goal is to artificially create infinitely long pipes or channels as to create fully developed turbulent flows, it is important to ensure that the length of the domain is sufficient to capture the long turbulent structures along the walls, as these are the main sources of the TKE exchange from the boundary layer to the outer flow, and gives the characteristic logarithmic flow-profile in Figure 2.4 [47]. To visualize these turbulence structures we used the λ_2-criterion (see Appendix B) to generate iso-surfaces of turbulent structures along the wall. Figure 4.11a shows these structures along the wall in the WM-C mesh colored by the magnitude of the vorticity. There are some long structures visible, but due to the low resolution it is difficult to further analyze this result.

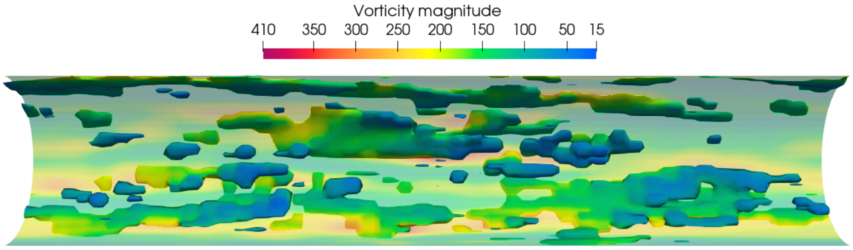

(a) Vortices near the wall in WM-C visualized with the λ_2-criterion.

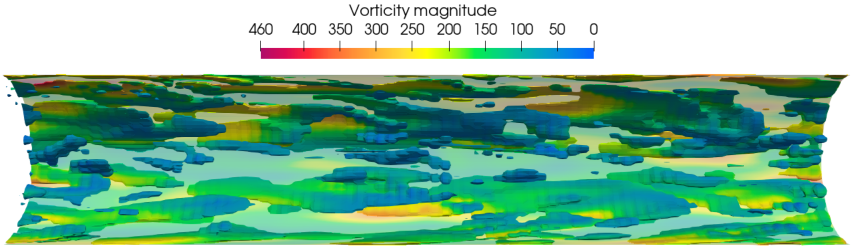

(b) Vortices near the wall in WR-F visualized with the λ_2-criterion.

Figure 4.11: Vortices near the wall in WM-C and WR-F. In (a) The poor resolution is due to the low resolution of the mesh. From this result, the length of the pipe seemed to be sufficient to capture long turbulent structures along the wall. In (b) the higher resolution of the mesh gives greater insight into the small overlapping "Q-events" produced by the slow moving velocity streaks along the wall.

The velocity streaks corresponding to the structures depicted in Figure 4.11b, are shown in Figure 4.12. We chose to plot the velocity with a color scale exhibiting greater contrast between the values. Here we can see slow moving velocity streaks which span the length of the pipe.

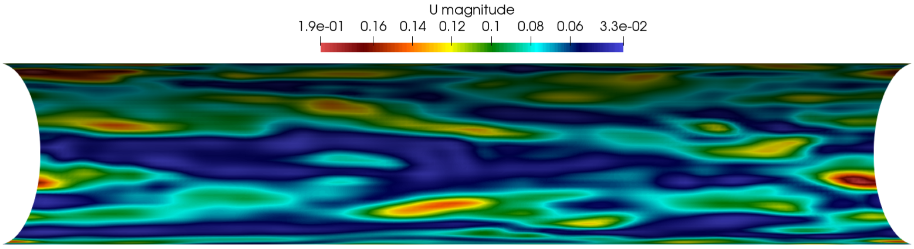

Figure 4.12: Velocity streaks near the wall in the same timestep as Figure 4.11b. The velocity is colored by a scale with greater contrast to better visualize the pattern of the velocity streaks near the wall.

Discussion and comparison against literature of the results from periodic turbulent flow in a pipe.

When studying the effects the choice of turbulence model had on the flow, we found that the employment of the Smagorinsky model led to rapid dissipation of spanwise perturbations, resulting in a notable diffusion of turbulence, while the WALE model demonstrated a more proficient handling of the transitional flow. After approximately 350,000 timesteps, it was evident that all non-streamwise velocities were entirely diffused out, leaving only a laminar profile in the streamwise direction, as depicted in Figure 4.7. The diffusive characteristics of the Smagorinsky model stem from its fundamental assumption that the subgrid-scale eddy viscosity ν_t is directly proportional to the local strain rate. Consequently, this formulation results in a non-zero viscosity at the wall, leading to an excessive damping of velocity within the boundary layer. In the context of turbulent and transitional flow, this excessive diffusion becomes problematic as it causes an overestimation of energy transfer down the energy cascade, which is represented by the modeled ν_t. The consequence of this overprediction is a pronounced damping of the turbulent motion in the flow near the wall, impeding the natural development of fully turbulent flow. This effect may be additionally pronounced for the performed simulation due to the low shear Reynolds number. Feldmann and Avila [48] found that the laminarization of turbulence in a pipe was very sensitive to the value of the Smagorinsky constant C_s for $Re_\tau = 180$. They found that the flow would laminarize for $C_s \geq 0.12$, while the optimal value for C_s approached the theoretical value for isotropic turbulence as Re_τ increased. Sensitivity analysis of the Smagorinsky constant was omitted for this thesis and was chosen as the default in OpenFOAM where $C_s = 0.167$.

In contrast, the WALE model exhibits significantly reduced diffusivity, thereby enabling the flow to evolve into a fully turbulent state more accurately. The WALE model better captures the complex interactions between the turbulent eddies, mitigating the issue of overestimating the energy transfer. Consequently, the WALE model provides a more favorable representation of turbulent and transitional flows by facilitating a smoother and more realistic transition to fully turbulent behavior. As a result, the WALE model proves to be a valuable alternative for this particular geometry, addressing the shortcomings of the Smagorinsky model and offering improved accuracy in simulating turbulent flow in a pipe. The significance of adopting appropriate turbulence models, such as WALE, becomes evident in scenarios where preserving the realistic flow dynamics is crucial for obtaining reliable and insightful simulation results.

Looking at the results from the global flow quantities, we saw that the utilization of wall models demonstrates superior accuracy in estimating the global flow quantities compared to the resolved boundary layer approach. Surprisingly, the coarsest mesh, WM-C, consisting of 93,960 cells, exhibits the most favorable outcome, with an error as low as 1.02% for Re_τ. In contrast, the WR-F mesh, consisting of 421,950 cells and employing a resolved boundary layer, yields a significantly higher error of 3.17%, surpassing WM-C by over three times. Turning attention to the results of the normalized shear velocity, presented in Table 4.3, WM-C consistently outperforms other meshes with an error of 1.46%, whereas WR-F exhibits a relatively higher error of 3.55%, approximately 2.4 times greater. A noteworthy observation from both Table 4.2 and Table 4.3, is that meshes utilizing wall models tend to overpredict the target values, whereas meshes with resolved boundary layers tend to underpredict them. The exact reasons underlying these discrepancies are not immediately evident. However, it is plausible that because the calculation of wall shear stress for wall models involves sampling a cell within the computational domain, which is subsequently applied as a Dirichlet boundary condition on the wall patch to compute ν_t [32], and as such the value for ν_t is calculated separately from the turbulence model, which we outlined in Section 2.5. Conversely, in the cases with resolved boundary layers, the value for ν_t at the wall is calculated by the employed turbulence model. These differences in the treatment of wall shear stress estimation may contribute to the observed variations in the accuracy of the predicted flow quantities.

Upon examining the mean axial velocity profile in Figure 4.8, it becomes evident that WM-C performs remarkably well in the Log-law region, outperforming WM-F and WR-F which both have a higher resolution. This behavior aligns with the expectations derived from WMLES, as a higher resolution may not be beneficial as long as the overall resolution is sufficient to meet the criterion of capturing 80% of the energy spectrum [32]. Not surprisingly, WR-F outperforms the other three cases in the buffer region due to the high resolution. As mentioned, mesh resolution in WRLES scales as $Re^{17/9}$, implying that higher-resolution wall-resolved meshes should yield more accurate profiles if the criterion of the resolution of the energy spectrum is met. This expectation holds true for WR-C and WR-F, as their increased resolution leads to improved accuracy, although WR-F is not entirely meeting the formal requirement of $Re^{17/9}$. Interestingly, using WMLES and WRLES causes under- and overprediction respectively. This holds for both levels of refinement. It should be noted however, that the DNS data from Yamamoto seems to capture the profile in Figure 4.8 marginally better than our simulations. Due to WR-F featuring similar cell count as Yamamoto and using an LES model, we excepted an increase in accuracy when using WR-F.

The RMS statistics and the only non-vanishing Reynolds stress in Figure 4.9, show similar characteristics as previously discussed. However, increasing resolution from WM-C to WM-F results in underprediction in the beginning of the Buffer Region in the axial RMS velocity in Figure 4.9a, while it results in overprediction in the radial and tangential RMS velocity in Figure 4.9b and Figure 4.9c respectively. Interestingly, the effect of increased resolution for wall modelling on the only non-vanishing Reynolds stress in Figure 4.9d appears to be negligible. The loss of accuracy in buffer regions when employing wall models was expected due to WMLES's assumption of a significant scale difference between the outer and inner layers, such that averaging of variables can be performed [49] [32]. Although typically necessitating a high Reynolds number and a coarse mesh to maintain this assumption [49], our adherence to best practices outlined by Mukha et al. [32] adopted to low Reynolds numbers where we placed the first cell-center within the buffer region as to prioritize the conservation of the geometrical features of the geometry, yields accurate results in the outer/Log-Law region, when compared to the DNS data from El Khoury et. al. [19] and Yamamoto [11]. Nonetheless, the inaccuracies in the WMLES simulations are most apparent in the axial velocity profile in Figure 4.8 and the RMS of velocity in Figure 4.9a. One potential cause for this could be the heightened susceptibility of velocity signals to aliasing errors due to the first cell's location and its intensity, relative to the radial and tangential velocities [49], particularly when the first cell center is at $y^+ < 50$, with the wall distance in the wall-parallel direction is sufficiently coarse. This is evident in the profiles of RMS of velocity in Figure 4.9a, Figure 4.9b, and Figure 4.9c, where errors are pronounced in the first cell center in Figure 4.9a. However, the subsequent points tend to adhere well to the profile from El Khoury et al.[19]. Remarkably, despite having only about one-fifth of the cells, the profile from WM-C, from the second point onward in Figure 4.9a, Figure 4.9b, and Figure 4.9c, adheres better to the profile from El Khoury et al. [19] compared to the profile from Yamamoto [11]. Furthermore, the profiles of the radial and tangential RMS velocity in Figure 4.9b and Figure 4.9c demonstrate negligible deviations in the first few cell centers for WM-C, with the overall profiles adhering well to the data from El Khoury et al. [19], considering the coarse mesh size.

In regards to Reynolds stresses, WM-C, WM-F and WR-C all underpredict the only non-vanishing Reynolds stress $\langle u_z u_r \rangle^+$ in Figure 4.9d, while WR-F exhibits a profile closely resembling the reference DNS data. The inaccuracies in the Reynolds stress can be linked to the inaccuracies in the axial and radial velocity components, depicted in Figure 4.9a and Figure 4.9b. Since the Reynolds stress is a product of these components, any inaccuracies therein would compound, leading to further discrepancies in the predicted Reynolds stress profile.

In the results from the mean and RMS velocity profile, depicted in Figure 4.10, we see good agreement between the data from Yamamoto [11] and the four analyzed cases. The overprediction in profile of the mean RMS velocity, may be caused by an underprediction of the data in Yamamoto's case, as all normalized components of the RMS velocity in Figure 4.9 is closer to the DNS data from El Khoury et. al. [19] in WM-C, WM-F and WR-F. There was no available data from El Khoury et. al. [19] for these two profiles, making a realiabe comparison difficult.

We created our pipe based on the study done by Yamamoto [11], to be able to perform an accurate comparative study although the length of the domain is short as it is on the lower end of the scale of best practices from the engineering world, and is shorter than what is found in literature, as summarized by El Khoury et. al. [19]. Nevertheless, we found that, as can be seen in Figure 4.11a and Figure 4.11b, the length seemed sufficiently long to resolve these structures. While there seems to be long structures in Figure 4.11b, there are smaller overlapping turbulent structures that are hard too see from a picture. In the literature, these wall-normal motions have traditionally been agreed upon as the main driving force behind the creation of velocity streaks [50] but as reported by Chernyshenko and Baig [50], new findings show that the main cause of the slow moving velocity streaks near the wall may indeed not be due to the wall-normal motions depicted in Figure 4.11a and Figure 4.11b, but rather through a combination of the mean velocity profile induced lift-up, the mean shear and the viscous diffusion. Nevertheless Jeon et. al. [51] showed a relationship between the velocity streaks and these wall-normal turbulent structures where long velocity streaks produced smaller overlapping "Q-events", which are vortex structures responsible for the transfer of TKE between the TBL and the outer regions of the flow, when visualized with the λ_2-criterion. The velocity streaks depicted in Figure 4.12 showed that there were streaks of low velocity towards the wall, which spans the length of the pipe. This is in line with the findings from Yamamoto [11], which explain the under-resolved data in Figure 4.9b and Figure 4.9c. Presumably, the pipe length is insufficient to capture the streak instabilities which are responsible for the exchange of TKE between the flow directions [51]. Since the pipe length is too short to accurately calculate the turbulent intensity, the transfer of momentum through turbulent kinetic energy from u_z^+ to u_r^+ and u_t^+ is underpredicted. This transfer of momentum is important in periodic flows, where the flow is driven by a momentum source in one direction.

4.3 Results for turbulent flow in helically coiled pipes

The simulations for the helically coiled pipes were performed, as mentioned, by mapping the fully developed flow from the outlet of WM-C to the inlet of the coils. To examine the results we cut evenly spaced slices normal to the flow direction in each coil, as depicted in Figure 4.13. Since the coils are increasing in length, the number of slices will also increase so that we get the same reference points in the three different cases.

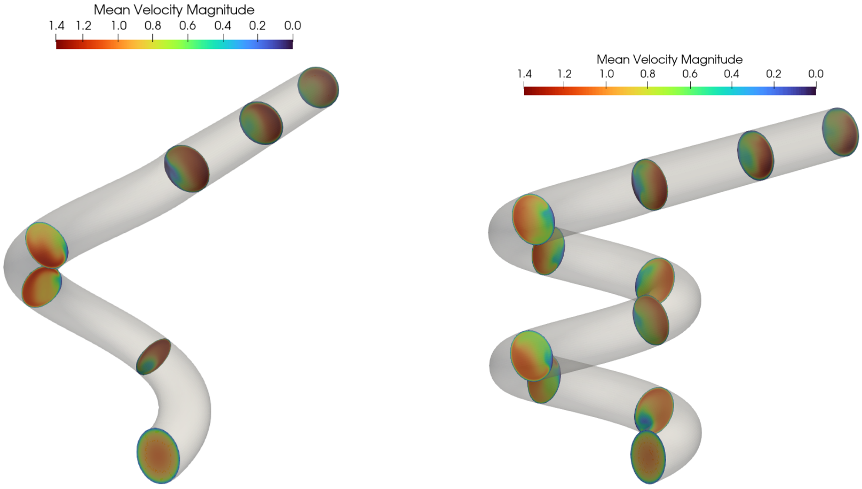

(a) Slices in C1. (b) Slices in C2.

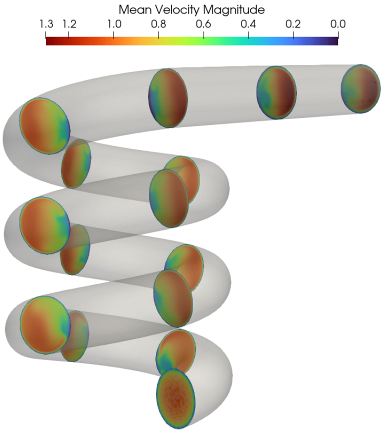

(c) Slices in C3.

Figure 4.13: Illustration of the location of the slices used for analysis in the three different coil configurations. To emphasize the location of these slices, they were plotted with the time-averaged velocity magnitude.

Velocity field

To examine the velocity in each of the slices we used the Turbulucid package (https://github.com/timofeymukha/turbulucid). The velocity plotted is the mean velocity normalized by the bulk velocity U_b of the WM-C pipe.

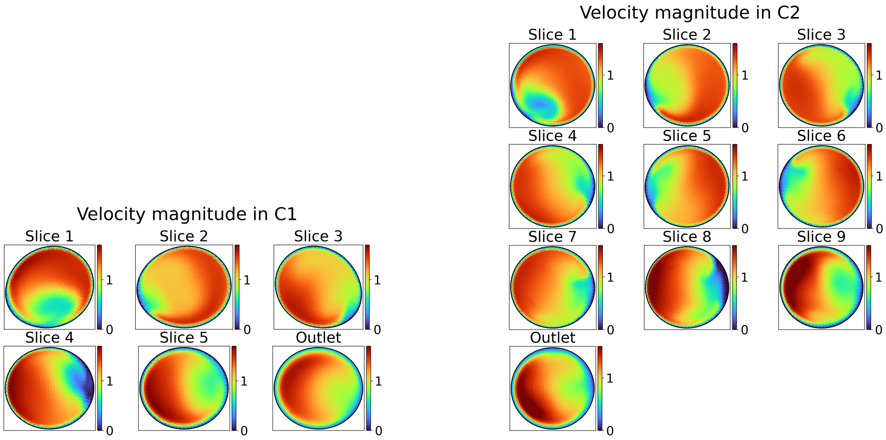

(a) Mean velocity field in C1. (b) Mean velocity field in C2.

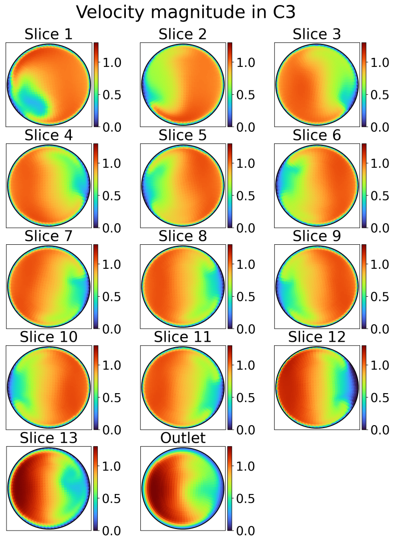

(c) Mean velocity field in C3.

Figure 4.14: Visualization of the mean velocity field in the three coils. (a) shows that C1 is too short for a stable secondary flow profile to develop, (b) shows that a stable secondary flow profile is established after two revolutions and (c) shows the stable secondary flow profile after two turns.

It is unfortunately evident that C1 coil became deformed in the creation of the geometry. We found that this was a shortcoming in the CAD program used. When profiles are swept along a helical path, there is a chance that it might deform. Nonetheless, the deformation is not deemed great enough to exclude the simulation from the examination.

The evolution of the velocity fields in Figure 4.14 exhibit some interesting characteristics. Most notably, the evolution of a stable secondary flow profile as seen in Figure 4.14c after Slice 6. As this slice is located right before the coil reaches two revolutions, it is not present in Figure 4.14a, and quickly disappears in Figure 4.14b as the flow exits the coil into the straight pipe outlet section. This secondary flow profile is due to the centrifugal force within the flow in helical coils, which has been well documented [3] [52], and is known as Prandtl's secondary flow of the first kind. It induces a return motion towards the wall on the inside of the coil [52]. This is due to the interaction of the pressure gradient and viscous forces inducing a centrifugal force across the cross-section, which moves the high velocity-area of a cross section towards the outer wall of the coil [53]. This effect is present in any cross-section, and thus the miss-shaped cross-section of C1 was deemed applicable for analysis.

The breakdown of the secondary flow is depicted in Figure 4.15 by streamlines colored by the time-averaged normalized velocity magnitude. The low velocity at the inner wall separates at the entrance of the outlet region. We can see that the secondary flow in the coil breaks down when entering the straight section, such that the streamlines become parallel with the wall.

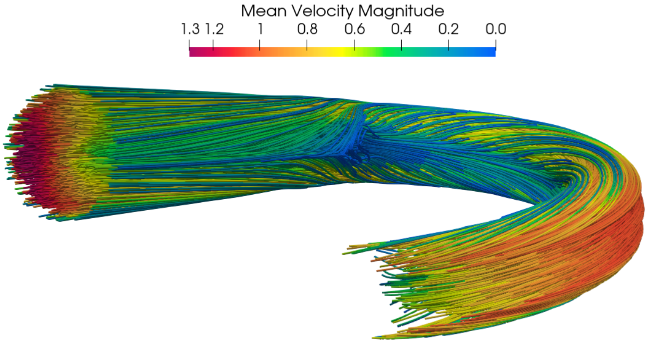

Figure 4.15: Streamlines of the breakdown of the secondary flow in C3 colored with the normalized mean velocity. As the secondary flow at the inner wall breaks down.

When sampling the velocity profile in C3 from the slices in Figure 4.14c in the vertical and horizontal direction, keeping the inner wall of the coil at the left-hand side throughout the geometry, we can see that the velocity profile in the horizontal direction quickly indicates a return-motion behavior. The velocity keeps decreasing towards the inner wall, while the velocity increases towards the outer wall. As the fluid enters the straight-pipe outlet in slice 12, the velocity decrease and increase becomes greater between slices. Similar behavior can be see in the vertical velocity profile, although to a lesser degree since, as depicted in Figure 4.14c, the velocity is the greatest towards the outer wall.

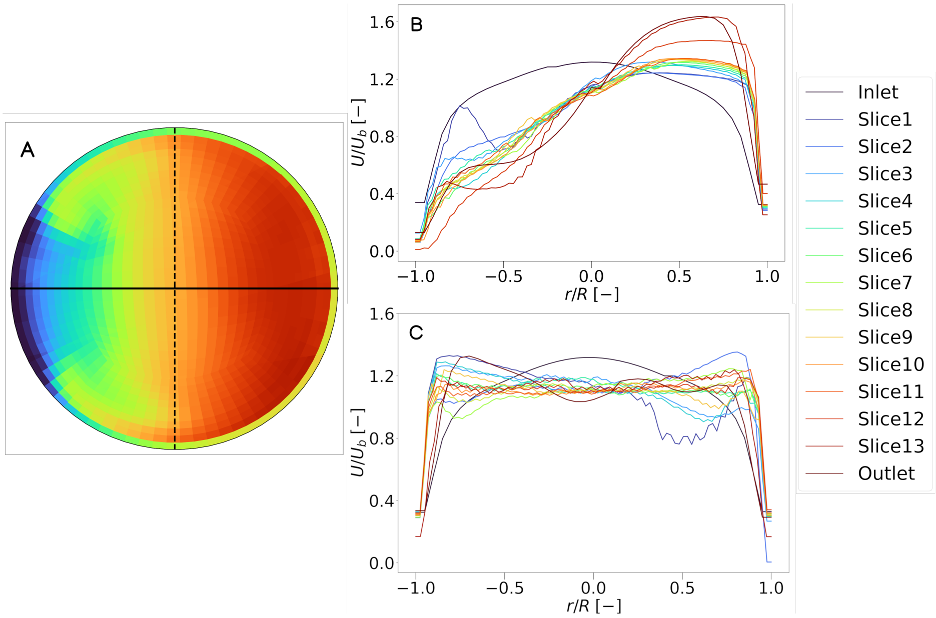

Figure 4.16: Time-averaged horizontal and vertical velocity profiles in C3 normalized with U_b. The velocity is plotted so that the left side shows the velocity at the inner wall of the pipe and the right side shows the velocity at the inner wall. The sampled lines are depicted in (A). The top plot (B) shows the vertical velocity profiles, sampled along the filled line (**-**), while the bottom plot (C) shows the horizontal velocity profile sampled along the dashed line (**- -**). The horizontal velocity shows that as the fluid flows through the coil, the velocity gradually increases at the outer wall, and decreases at the inner wall.

Pressure

In this subsection, measurements of the pressure are performed using the presented slices, which are subsequently used for sampling the horizontal pressure gradient within each cross-section. Depicted on the left-hand side in Figure 4.17 one can see that a spanwise pressure gradient is present across the cross-section. The pressure is peaking at the location of where the secondary flow develops. Looking at the difference in pressure sampled along the same line as in Figure 4.16. In the horizontal direction, we can see a pressure drop across the cross-section as well as a gradual decrease in overall pressure in the slices as the flow travels through the coil. The pressure is normalized by the area-averaged pressure of the inlet such that $p_0 = \frac{1}{A}\int pdA$. The pressure gradient across the sample-line seems to stabilize to a constant value at Slice 3, before it decreases sharply when to flow enters the straight outlet section.

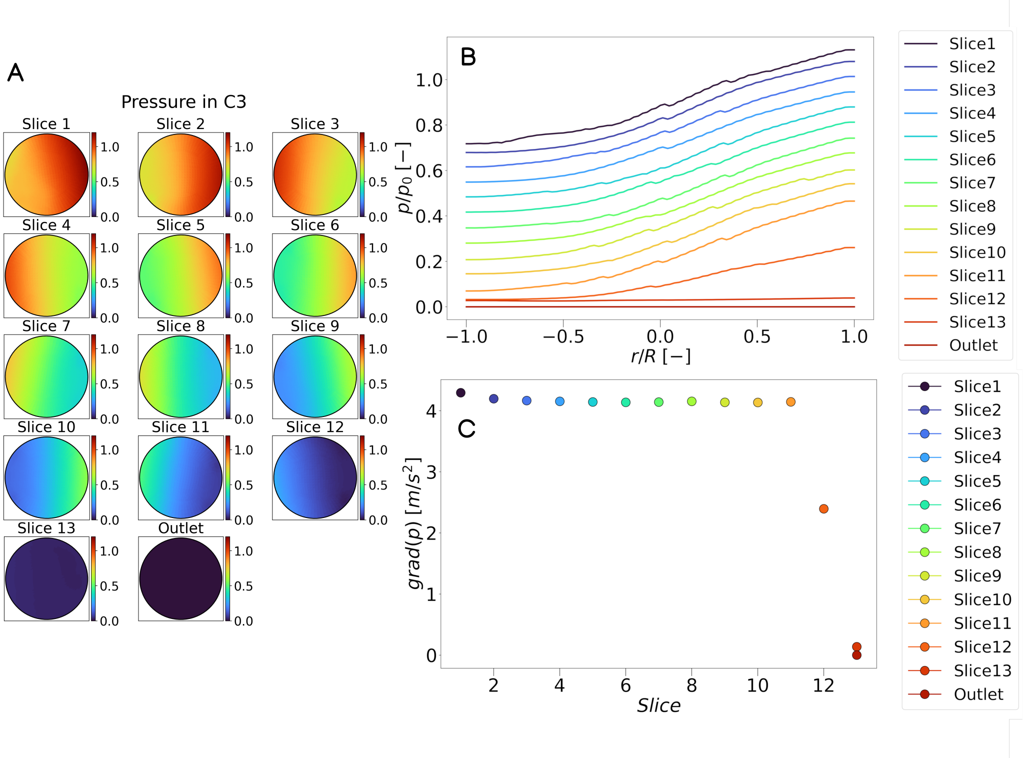

Figure 4.17: Pressure distribution in C3. The slices on the left-hand side (A) show the pressure in the sampled slices. The top plot on the right-hand side (B) show the decrease in the normalized pressure sampled along a horizontal line in the cross-sections depicted on the left. The orientation is such that the left side of the plot is towards the inner wall, while the right side is towards the outer wall. The overall pressure in the slice decreases as the fluid moves through the coil, reaching zero at the straight pipe section. The plot at the bottom right (C) shows the gradient of the pressure in the horizontal direction. The gradient reaches a stable value after one revolution.

These same characteristics can be observed also in C1 and C2, depicted in Figure 4.18, although there is a quicker drop in pressure due to the shorter length of the coil. Notably, the stabilized pressure gradient in C2 differs little from the pressure gradient in C3. The measurement of the pressure gradient in C1 however, does not reach a stable value due to the coil only having one revolution.

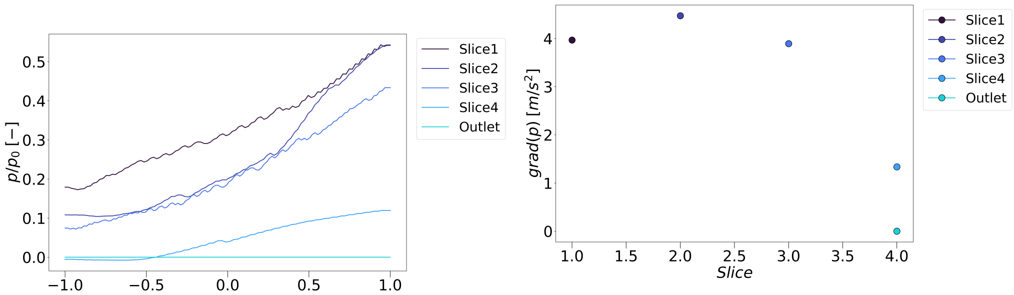

(a) The pressure across a horizontal line in each of the sample slices, in C1

(b) The pressure gradient across a horizontal line in each of the sample slices, in C1

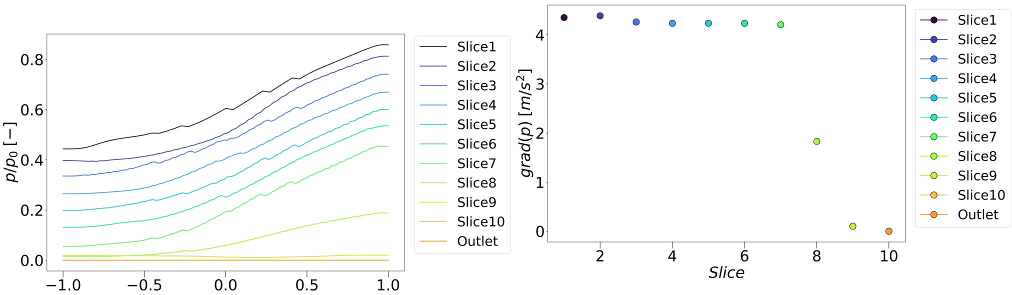

(c) The pressure across a horizontal line in each of the sample slices, in C2

(d) The pressure gradient across a horizontal line in each of the sample slices, in C2

Figure 4.18: Measurements of the spanwise pressure and pressure gradient in C1 and C2. (a) and (b) show that in C1, the coil was too short to give an accurate measurement of the pressure and the pressure gradient. (c) and (d) on the other hand, show that the pressure gradient reaches a stable value after one revolution in C2, in line with the findings in C3. The spanwise pressure gradient also shows similar characteristics to C3.

Turbulent kinetic energy

Examining the TKE in C1,C2, and C3 depicted in Figure 4.19, it is evident that as the fluid flows through the coil, the TKE diffuses, and when it enters the outlet-section we can see an increase in TKE again, indicating a transition to turbulent flow. The increase of TKE in the outlet-section seems to depend on the number of turns in the coil, as the TKE in the outlet-section of C3 is lower than C2, which in turn is lower than C1. The peak of TKE is seemingly located halfway through the first revolution, after which there is a decrease in TKE until the flow enters the straight outlet section. In each of the slices within the coil, the peak of the TKE is located along the outer wall of the coil, while the TKE at the inner wall is shifted towards the inner region of the cross-section.

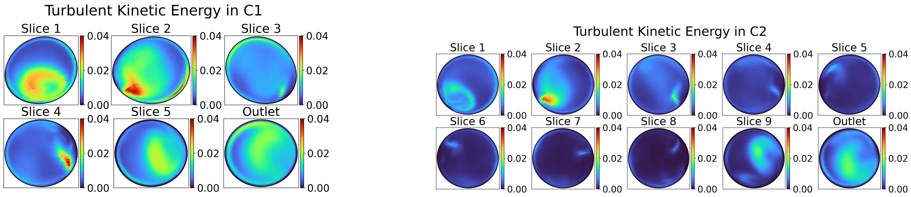

(a) TKE in C1.

(b) TKE in C2.

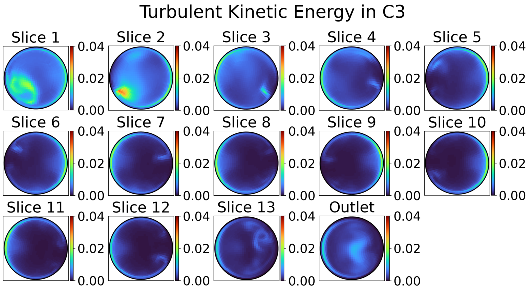

(c) TKE in C3.

Figure 4.19: TKE in C1, C2, and C3 plotted such that all three figures share the same scale. The TKE in C1 in (a) exhibits different characteristics than the TKE in C2 and C3 due to the malformed geometry. (b) and (c) show that the TKE diffuses as the fluid moves through the coil, and increases again in the straight pipe outlet, which is inline with the findings from Viswanath et. al. [5].

Aforementioned, in LES the aim is to resolve 80% of the energy spectrum to accurately capture the fluid motion. For geometries where there is an increase and a subsequent decrease in TKE, more consideration may go into grid creation than for a geometry with easily indistinguishable energy-regions such as a pipe or a channel. To evaluate the resolution of the grid, we used the ratio of the resolved TKE to the total TKE η from Equation (3.3), depicted in Figure 4.20. We can see that as the fluid flows through the coil, less and less of the energy spectra is resolved. This leads to an underprediction of the TKE in the coil, as in some areas the percentage of the resolved energy goes down to 40% of the total TKE. The resolution seems sufficient in the due to the decrease in TKE in the middle of the coil.

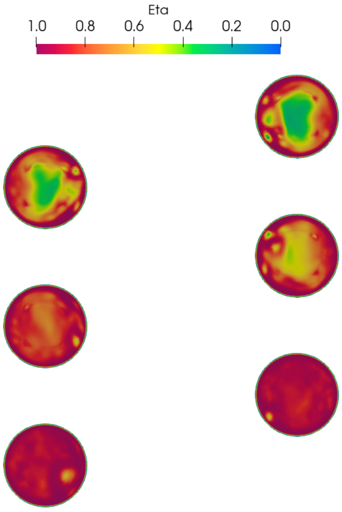

Figure 4.20: Captured energy spectra in C3. Due to the shifting of the location of the maximum velocity towards the outer wall and consequently the shifting of high TKE areas, the resolution of the mesh is not sufficient to capture 80% of the energy spectrum, leading to increased artificial diffusion.

We further investigate this effect by measuring the TKE throughout the coil and comparing it to DNS data, as presented in Figure 4.21. Here the TKE is measured by performing an areal integral, such that $k = \int_A k dA$, which is normalized with the area integral of the TKE at the inlet. The x-axis represents the slice index. Upon inspection, it is possible to see that the overall TKE is underpredicted in C1, C2, and C3 compared to the DNS data from Yamamoto [11]. The result in Figure 4.21b shows similar characteristics as Figure 4.21a, with the peak of the TKE located right after the first turn in the coil and an increase in TKE at the straight outlet section. The amount of TKE within the coil is seemingly dependent on the curvature and torsion, with C1 exhibiting the most TKE, while the difference between the amount of TKE in C2 and C3 being lower. C2 and C3 exhibit similar rates of diffusion of TKE, while this rate is difficult to quantify for C1 due to a lower amount of sampling points, due to its shorter size.

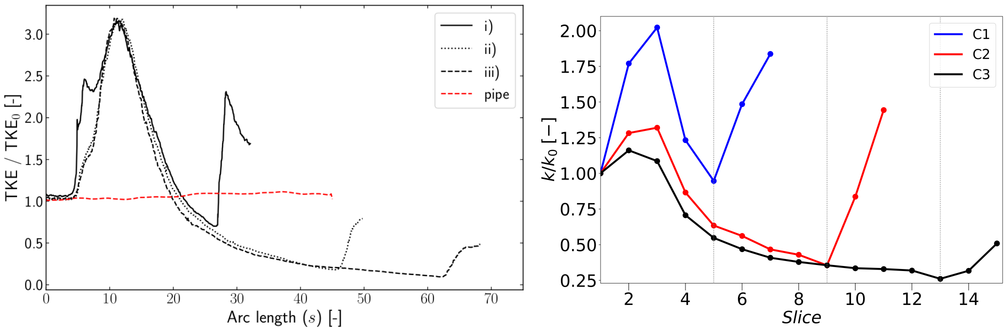

(a) TKE from Yamamoto[11].

(b) TKE in C1, C2 and C3.

Figure 4.21: Comparison of normalized TKE in C1, C2, and C3 to the DNS data from Yamamoto [11]. The three horizontal dotted lines represent each turn of the coil. It can be seen that the overall TKE is underestimated in each of the coils compared to similar coil geometries from Yamamoto [11].

Dean vortices

For flows in curved geometries, secondary flows are superposed on the flow due to the centrifugal force exerted on the main flow. The expected flow pattern is two counter-rotating vortices at opposing sides of the cross-section, such that the low velocity flow from the interior side of the coil flow towards the higher velocity at the outside wall, where the there is an increased centrifugal force which again causes a return motion to the interior wall as depicted in Figure 4.22.

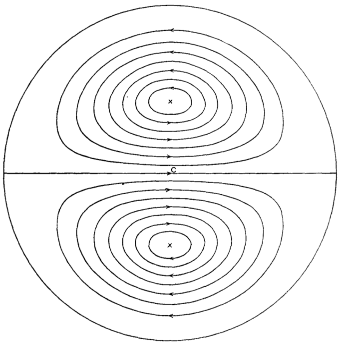

Figure 4.22: Schematic of two counter-rotating Dean vortices in the cross-section of a curved pipe [3].

Visualization of the mean Dean vortices in C3 using Line Integral Convultion (LIC) is presented in Figure 4.23, overlayed with the mean velocity magnitude. Evidently, the turbulent eddies from the inlet are dissipated into two main Dean vortices already in Slice 3 which is right after the location of the maximum TKE and is located in 3/4 of the first revolution. Although, four vortices appear again in Slice 4. Furthermore, The symmetry of the Dean vortices is not kept throughout the domain, as the center of the lower vortex is not stationary in relation to the upper vortex.

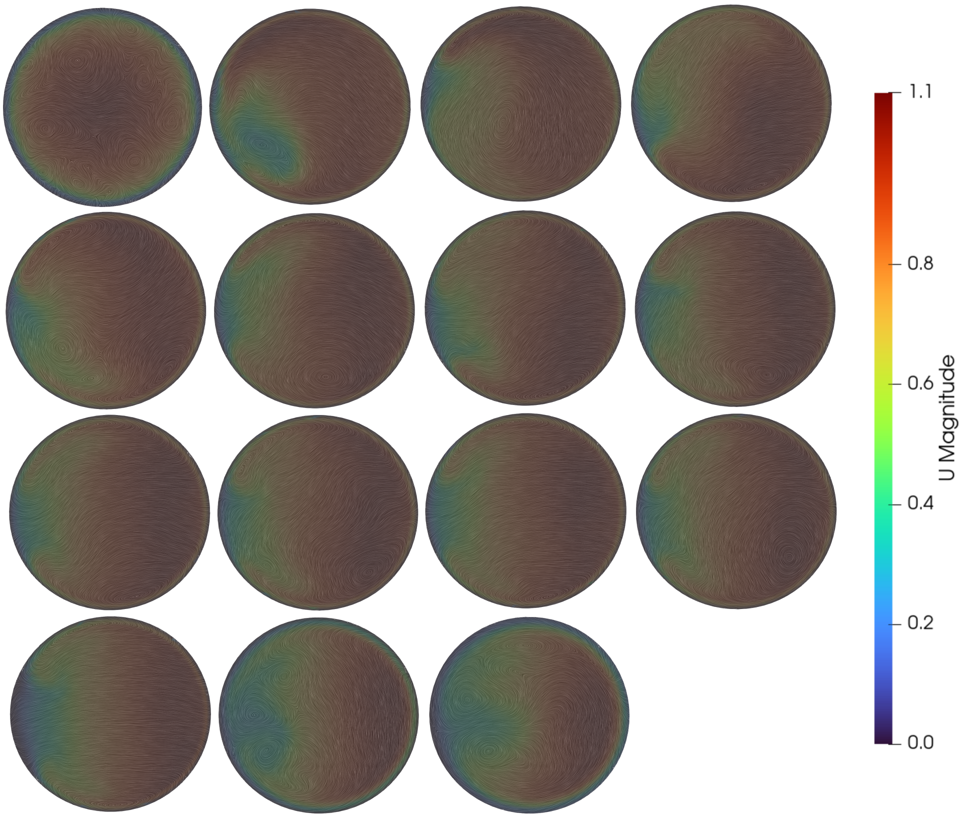

Figure 4.23: Line Integral Convolution (LIC) of the mean velocity in C3, showing the evolution of dean vortices throughout the coil.

By further examination of the instantaneous Dean vortices in Slice 13, where the flow exits the coil, we can see that, although the mean velocity field indicates two vortices, multiple vortices with varying strength and location appear at what appears to be random time-intervals. In Figure 4.24 the bottom plot shows the vortices from the mean velocity field using LIC and the planar velocity vectors normalized with the bulk velocity, the two upper plots are from random time steps. It is evident that the number of vortices in the mean flow, is not representative of the number of instantaneous vortices. The upper-left plot shows four vortices, two on the upper-half close to the wall and two on the lower-half close to the wall. The upper-right plot once more shows four vortices. Two of these are located symmetrically on the upper- and lower-half. Additionally there is two counter-rotating vortices located along the horizontal centerline, at the location of the maximum mean velocity in the main flow.

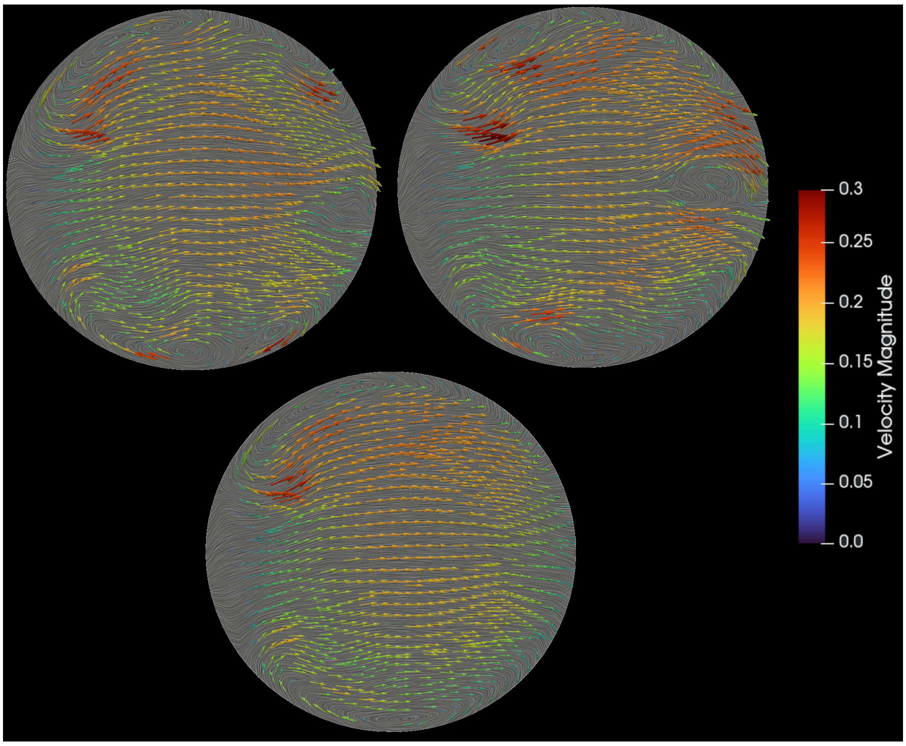

Figure 4.24: Surface plots done using LIC and surface vectors of two instantaneous velocity profiles on the top, and the mean flow on the bottom. The instantaneous velocity shows the appearance of multiple vortices not captured by the mean velocity.

Discussion and comparison against litterature of the results for turbulent flow in helically coiled pipes

In the velocity field of the coil, presented as sampled slices, we saw that the peak of the velocity moved towards the outer wall. When the fluid reached the end of the coil where it enters a straight outlet section, it separates from the wall possibly due to the decrease of the pressure in the straight section. As there is no spanwise pressure gradient present, due to the geometry shifting to a straight pipe, the effect of the induced centrifugal force disappears. This causes the secondary flow to break down, as the high-velocity towards the wall slowly moves towards the center of the pipe, where it is expected to stabilize after a certain length. We suspect that a further increase of the length of the outlet section will give greater insight into this behavior, as the flow would have more time to stabilize.

In the streamlines at the outlet of C3 in Figure 4.15, we observed a separation of the flow along the inner wall in the pipe when it entered the coil, which may be due to the increase of wall shear stress at the outer wall from the sharp change in curvature when the geometry is no longer being effected by a centrifugal force. Furthermore, we saw that the streamlines gave greater insight into the development of the flow in the coil. As indicated by the velocity fields in Figure 4.14, the fluid flows from the outer wall into the inner wall, in a stable twisting motion. This flow characteristic is favorable in engineering applications, as helically coiled pipes are deemed as a better candidate for heat transfer than straight pipes due to not only the larger surfaces area of heat transfer through diffusion, but also due to convection of temperature caused by the secondary motion in the coil.

The pressure in the coil is expected to decrease as the fluid flows through it. Mentioned by Kumar in [53], one of the main drawbacks of using helically coiled heat exchangers is the increased pressure difference over the coil (from the inlet to the outlet) compared to a straight pipe heat exchanger, which increases the required pump power to drive the flow at a favorable flow rate. Even though pressure-measurements from an incompressible simulation have no direct physical relation, we observed that the pressure difference between the inlet and the outlet of the coils increased with the length of the coil.

Although the pressure in itself cannot be related to physical phenomena, the pressure gradient can. Seen in Figure 4.13c, the pressure gradient across the cross-section is what is causing the secondary motion of the flow. Usually, the centrifugal force exerted on the flow in helically coiled pipes is expressed as being balanced by the pressure gradient [54] [53], while in fact it is the pressure gradient induced by the fluid constantly hitting the wall which is balanced by a centrifugal force. In accordance with the previously discussed centrifugal force, the pressure gradient across a cross-section should be expected to be constant within the coil as it is directly proportional to the centrifugal force exerted on a coil of a specific curvature. We saw that, in Figure 4.17 and Figure 4.18, the value of the pressure gradient became constant in C3 and C2 after one revolution, although the curvature and torsion of these geometries are different. This further strengthens the possibility that the centrifugal force exerted on the flow arises mainly due to the curvature of the coil and thus curvature seems to be the parameter of significance for helically coiled pipes.

However, this is not a surprising result as the centrifugal force is directly a function of the curvature. This was also observed by Hüttl and Freidrich [55], Ciofalo et. al. [56] and Yamamoto [11]. Ciofalo et. al. [56] found that increased curvature led to a significant increase of heat transfer rates as well as frictional losses, where as increased torsion did not have an significant impact on these quantities. These are favorable geometrical characteristics for a heat exchanger, as one needs only to increase the radii of the coils to increase heat transfer rates. This makes helically coiled heat exchangers ideal for internal and external heat exchanger of finite height, as depicted in Figure 1.1.

The TKE was found to not reach the criterion from Pope [23], wherein a LES simulation should resolve 80% of the energy spectrum. We visualized this using the ratio of resolved and modelled TKE, depicted in Equation (3.3). This under-resolution increases the diffusion, as ν_t is overestimated, while the resolved TKE is underestimated. The under-resolution of the grid caused inaccuracies in the TKE when comparing the findings to that of the DNS data from Yamamoto [11], although the location of the peak of the TKE and an increase in TKE in the straight outlet section exhibited similar behavior. The sharp increase in TKE in the straight pipe outlet section in C1 and C2 depicted in Figure 4.21b can be attributed to not only the findings from Viswanath et. al. [5], but also that here the grid size is sufficient to resolve 80% of the energy spectrum, as it is in the periodic pipe in Section 4.2. The underlying phenomenon seemingly responsible for this behavior, is the shifting of the high-energy region from the walls of the domain towards the inner region of the coil where there is a peak of the resolved TKE in Slice 1 and 2. This increases the necessity for a higher resolution in the middle of the domain where the smaller eddies are located. Illustration of this behavior can be understood by examination of the underlying reason for a formal high resolution requirement in LES. The criterion relies on that the smaller eddies within the flow should be sufficiently resolved, typically located along the wall as depicted in Figure 4.25. Here the smaller eddies are located along the wall, and hence the grid is refined towards to wall. However, since wall modelling is used in the simulation of the coils, which circumvents the need for near-wall resolution, and there is a high-energy region within the coil away from the walls, a higher resolution is needed to accurately represent the size of the eddies within the low-energy region similarly to what is depicted in Figure 4.25. This is counter-intuitive when the classical resolution scaling for WMLES, estimated purely based on the Reynolds number, is used to asses sufficient grid resolution. Furthermore,

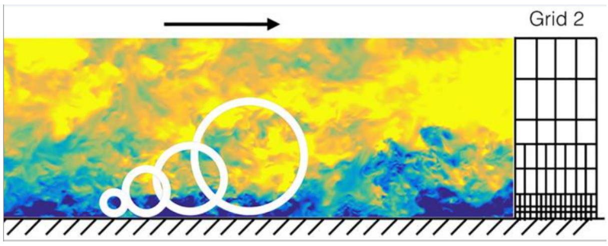

Figure 4.25: Resolution requirement due to the eddy size, borrowed from Lozano et. al. [57]

due to the fundamental assumptions of wall models, as presented in Section 2.5, where a single function representing the boundary layer of the whole domain is obtained and thus an equilibrium is assumed. The flow is assumed to be parallel to the wall, not affected by pressure gradients and without acceleration. This assumption may not hold for geometries such as helical coils due to the secondary flows and subsequently a spanwise pressure gradient. This may cause unknown discrepancies in the result, as summarized by Larsson and Kawai [58].

The underresolution of TKE may indicate that the use of wall models and a corresponding coarse mesh resolution in a domain where the location of the peak of TKE is away from the wall in some regions, may lead to increased diffusion. Further examination of this result can be done by looking at the implementation of ν_t in OpenFOAM (see Equation (2.17)) and the transport equation of the resolved kinetic energy

$$\frac{Dk_{res}}{Dt} - \frac{\partial}{\partial x_j}\left[\bar{u}_i\left(2(\nu+\nu_t)\bar{S}_{ij} - \tau^r_{ij} - \frac{\bar{p}}{\rho}\delta_{ij}\right)\right] = -\epsilon_f - \mathcal{P}_r, \tag{4.1}$$

where ϵ_f is the viscous dissipation of the kinetic energy in the resolved field

$$\epsilon_f = 2(\nu+\nu_t)\bar{S}_{ij}\bar{S}_{ij}, \tag{4.2}$$

and $\mathcal{P}_r$ is the rate of production of the unresolved kinetic energy

$$\mathcal{P}_r = -\tau^r_{ij}\bar{S}_{ij}, \tag{4.3}$$

such that $\mathcal{P}_r$ represents the rate of transfer of energy from the resolved to the unresolved scale [23]. τ^r_{ij} is the residual stress tensor

$$\tau^r_{ij} = -2\nu_t\bar{S}_{ij}. \tag{4.4}$$

As evident by the sign of ϵ_f and $\mathcal{P}_r$ for eddy viscosity models as $\nu_t > 0$, there is no backscatter (transfer of energy between the resolved and unresolved scale), thus they both appears as sinks in Equation (4.1). For situations where k_{sgs} is more than 20% of the total TKE, the energy of the resolved eddies k_{res} in the coil, dissipates faster than expected due to the overestimation of ν_t, as evident from Equation (2.17), when the grid resolution is not sufficient. In a geometry such as a helical coil where there is diffusion of turbulence, a fine enough grid to resolve the eddies at the point where there is a maxmimum of TKE may be beneficial to use for the whole domain due to the unconventional distribution of TKE. How much the solution is impacted by underresolution in implicit filtering, can be represented by looking at a plot of the energy spectrum, where the numerical error introduced by implicit LES is emphasized. In Figure 4.26 the area under the curve to the left of the dashed vertical line represents the resolved TKE, while the area under the curve on the right represents the unresolved TKE. k_c is analogous to the gridsize when recalling that the characteristic size of all the eddies within a cell is represented by a mean, which we chose to be $\Delta = \sqrt[3]{V_{cell}}$, whereas k_c is the wavenumber of the largest unresolved eddy. The figure is borrowed from Bull and Jameson [59], where they showed that implicit filtering in LES may cause a steeper drop off in the resolved TKE due to numerical errors. This is presented as the area between the dashed parabolic line and the dashed vertical line, labelled "num. error". Additionally, recalling

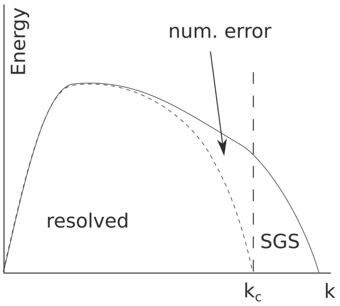

Figure 4.26: Energy of the turbulent eddies plotted over the wavenumber. k_c representes the cutoff-wavenumber i.e. the wavenumber of the smallest resolved eddy [59].

that a LES simulation should capture atleast 80% of the energy spectrum, when the captured energy is as low as 40%, as depicted in some areas in Figure 4.20, the resolved TKE will be heavily underpredicted when factoring in numerical errors.

It should be noted however, that the resolution of the grid may not be the cause of these descrepancies. Instead, it could be contributed to the validity of using the WALE model in such a complicated flow scenario. There is no sensitivity study done on the effects the model constants, C_w and C_k, have on the result and that imbalance in energy comes from the fact that the calculation of k_{sgs} is not valid in such a scenario, leading to an overestimation of ν_t, which reduces the amount of resolved TKE in the domain. The original authors of the WALE model reported that; "*In the case of a laminar flow with a more complex 3D velocity gradient, there is no evidence that the WALE model (or any other SGS model) will give a reasonable answer.*" [30] (p. 198)

Eventhough we observed descrepancies in the solution, the effect off the torsion and curvature on the turbulence is still possible to interpret from the differences in the solution between the three geometries. The torsion has been shown to be the geometric parameter that enhances turbulence in coils as it increases, while the curvature suppresses it [11] [60] [8]. The difference in curvature and torsion between the coils, seen in Table 3.4, can be calculated by their difference in percentage seen in Table 4.4. Here the decrease in torsion is reflected in the decrease in the TKE from Figure 4.21b, where there is a large difference between the TKE in C1 and C3. The small difference between C2 and C3 in the curvature, and the larger difference between C1 and C2, are in line with the similar rates of diffusion.

Cases	κ [%]	τ [%]
$C1 - C2$	19.6	−45.0
$C2 - C3$	3.8	−45.6
$C1 - C3$	24.2	−70.6

Table 4.4: Difference in curvature κ and torsion τ in percentage between C1, C2, and C3. Negative percentage indicates a decrease while a positive percentage represents increase. The increase of curvature is greater between C1 and C2, than between C2 and C3, while the decrease in torsion between C1 and C3 is greater than that of C2 and C3.

The Dean vorticies observed in the coils can be characterized by the Dean number De from Equation (2.25), such that a baseline for their effect can be stipulated for a particular geometry. For a coil with $Re = 5300$ and $R_c = 3R$ we get $De \approx 3060$. From an extensive experimental study of flow in a 90° bent pipe, Kalpaki [9] found that the most significant parameter for the Dean number was the curvature ratio D/R_c for $2.7 \times 10^4 \leq Re \leq 8.7 \times 10^4$. Nashine et. al. [61] found that an increase in the Dean number is favorable for heat transfer in helical coils, which is in contradiction with the findings in Section 4.3 where the dissipation of the TKE was found to be correlated to the curvature. Due to the favorable effect turbulence has on convected heat transfer due to the mixing of the fluid, there seems to be a missing relation between the TKE, Nusselt number (the ratio of the convective to the conducting heat transfer), curvature, and torsion. This is further backed up by the findings and summarization from Ferng et. al. [62], where a strong correlation between the Nusselt number [63] and the Dean number was found. Furthermore, Ferng et. al. [62] additionally showed that there is also a correlation between the pitch, and therefore the torsion of the coil and the Nusselt number which obscures the relation of curvature and torsion to the efficiency of a helically coiled heat exchanger. It could be stipulated that, since the Dean number is independent of the torsion, the structured Dean vortices are more beneficial for heat transfer than that of turbulent flow. This is however out of the scope of this thesis.

Yamamoto [11] found that the Dean vortices had a destabilizational effect on the flow, causing the smaller eddies to dissipate. Consequently, the amount of fluctuation in the velocity field will reduce and thus the TKE will be reduced. It was reported that, due to the increase of rotation in the flowfield when the fluid first enters the pipe caused by the imbalance of the centrifugal force and the pressure gradient, there will be an increase in TKE along the first bend of the coil. These simulation where done using finite element method on meshes where the cell count was approximately one order higher. It is therefore interesting to see if we succeeded in capturing similar flow features to that of Yamamoto [11]. As can be seen in Figure 4.23, the expected symmetry of the Dean vortices is not present in the whole domain. This may be due to the critical value for the Reynolds number as presented by Dean [3], where the relatively high Reynolds number for a coil where $R_c = 3R$ struggles to relaminarize the flow. The behavior of Dean vortices in turbulent flow is not as extensively studied, therefore litterature on wether the Dean vortices stay symmetrical and vary in time is unanswered [64]. We found no literature on this behavior of Dean vortices in helically coiled pipes, but it is well documented in bent and toriodal pipes where it is referred to as swirl switching [64] [65] [66]. In the literature on bent pipes, the turbulent flow has been generated either with a periodic pipe [64], as employed in this thesis, or using a Divergence-Free Synthetic Eddy Method [65] [67]. Hufnagel et. al. [65] summarized that the effect of using a Divergence-Free Synthetic Eddy Method boundary condition for the inlet as opposed to the traditional method of recycled turbulence, had no effect on the appearance of swirl switching, whereas earlier studies found that it was directly a consequence of the long velocity streaks in the periodic pipe, shown in Figure 4.12. Swirl switching was attributed to a large three-dimensional wave caused by the bend in the pipe. Tunstall and Harvey[66] found that this is caused by the shedding of the shearlayer close to the inner wall. The continuous bend of a coil, although less steep than that of Tunstall and Harvey [66] may cause small eddies to appear in the instantaneous flow due to the shedding of the shear layer, whereas the intensity and irregularity of these eddies cause them not to be visible when performing a time average of the flow. Our findings showed that examination of instantaneous velocities may exhibit more, although weaker vortices. These vortices appeared at irregular intervals with varying size and location.

CHAPTER 5

Conclusion and future work

5.1 Conclusion

In this thesis we have investigated how LES simulations can be optimized in complex flow scenarios. A variety of factor have been considered, such as a comparison between the classic Smaroginsky model and the improved WALE model, the accuracy of wall modelling in LES at a low Reynolds number, and the resolution requirement for LES in complex flow.

Firstly, much time was spent optimizing the mesh geometry for the pipe for use with LES turbulence models. We utilized two different industry-standard meshes and proposed a third one as an improvement. The literature on meshes for turbulent flow in pipes proved lacking, as the process of meshing is often not reported, despite their significance and the fact that they may make up a majority of the work associated with a simulation. We conducted a detailed examination of what constitutes an optimal mesh used in FVM codes. Different geometrical parameters and their effect were discussed, where we found that of the parameters investigated, the skewness of the cells in the boundary layer seemed to affect the solution negatively. Errors due to skewness in meshes cannot be circumvented using simple numerical techniques, and as such are prone to a simulation being reduced to the "GIGO" (Garbage in, garbage out) phenomenon. The mesh we proposed as a solution to the high skewness in the boundary layer showed reduced skewness, while the non-orthogonality in the central region were much higher in the corners than that of the preceding two. This increased non-orthogonality showed not to be crucial for the accuracy, as it can be reduced using extra inner loops in the PISO algorithm. When the skewness in the boundary layer was high, it led to discrepancies in the solution, resulting in an increase in wall shear stress in specific areas. Consequently, streaks of wall shear stress were observed to align with the geometric features of the mesh rather than occurring randomly. This observation indicated discrepancies in other variables, such as the TKE.

Upon investigation of the performance of two different LES models on the transitional flow in the pipe, we found that the overly diffusive nature of the classical Smagorinsky caused the spanwise perturbations to be diffused out, rather than driving the evolution of fully turbulent flow. The improved WALE on the hand quickly became turbulent and was chosen to be the best of the two without performing a sensitivity analysis of the Smagorinsky constant.

The simulations conducted to estimate the accuracy of WMLES in a pipe at a low Reynolds number included two different resolution of the meshes for both WMLES and WRLES. These were compared to the results from similar simulations conducted using DNS with two different numerical techniques. Not surprisingly, the effect of raising the resolution in a wall modelled mesh where the criteria of resolved energy is met, is not necessarily favorable, as backed up by the findings in the literature. The wall-resolved simulation however, showed an increase in accuracy when the resolution was drastically increased, reaching that of the DNS data. The results from our LES simulations showed superior accuracy over the DNS comparison data in both wall-modelling cases, as well as with the wall-resolved mesh which had approximately the same number of cells used in the comparison data.

Due to sufficient accuracy from the coarsest wall-modelled mesh, WM-C, it was used to sample inlet data for the helically coiled pipes. The effect this had on the result in the helically coiled pipes was not measured, however, the flow exhibited expected features. We observed secondary flow phenomenon as well as a decrease of turbulence through the coil, and an increase in turbulence in the outlet section. We performed measurements of the velocity field and pressure gradient which showed that a constant centrifugal force acted on the coil due to the constant curvature for a given geometry. Furthermore, increased torsion were shown to have an impact on the production of turbulence while the curvature had an effect on the rate of dissipation.

We observed that when performing LES simulations of a coil, the mesh requirement is higher than that of the periodic pipe used for inlet data. As the turbulence dissipated throughout the coil, finer mesh may be required to continuously resolve 80% of the energy spectrum. This gave an inaccurate estimation of the turbulence in the coil in comparison with DNS data.

Inspection of secondary flow phenomenon within the analyzed coil geometries revealed the existence of both Prandtl's secondary flow of the first kind and Dean vortices. We showed that the former was a crucial feature for the mixing of the fluid within the coil, as low-velocity fluid were constantly transported from the inside-wall of the coil to the high-velocity outer wall. Upon comparison against literature, this effect was emphasized as a favorable feature for convected heat-transfer.

Dean vortices were created due to the aforementioned flow feature. These appeared as two counter-rotating vortices towards the top- and bottom-wall of the cross section. The location of these vortices in the mean flow were placed at different locations depending on how far the flow had traveled throughout the coil. They sometimes appeared asymmetric within a cross-section such that one could be towards the wall while the other would appear in the middle of its respective side of the cross-section. Inspection of the instantaneous velocity showed that taking the mean of turbulent flow in coils, may not accurately represent the flow behavior, as we saw that more vortices appeared, with varying strength and location, at random intervals. Their effect on the dampening of the turbulence was evident, although the phenomenon of increased turbulence when entering a straight pipe may be caused by the instantaneous instabilities. Moreover, we saw the appearance of a separation point of the flow when it entered the straight pipe, which may further amplify the increase in turbulence.

5.2 Future work

In the investigations conducted in this thesis there is much room for improvement and additional work to be done. First of all, the meshes created for the pipe, although done by testing a large number of different configurations, may be further improved upon by constructing a mesh similar to that of El Khoury et. al. [19], where the cross-section is separated into 12 regions instead of five. This may lead to further reduction of the skewness and non-orthogonality in the mesh and thus increased accuracy, although at an increased cost to labour, which may not be feasible outside of research purposes. There should also be conducted investigations of different meshing methods than a pure hexahedral domain. In recent years, polyhedral meshes have gained popularity due to their computational efficiency. They have shown to be on par with pure hexahedral meshes using LES models, while greatly reducing the computational cost [68] [69]. They also exhibit lower skewness and non-orthogonality due to their geometric shape. Polyhedral meshes are however, more common in commercial solvers, as the existence of open-source meshing algorithms are hard to come by. Furthermore, the pipe itself should be extended greatly so that all of the slow-moving velocity structures are captured sufficiently. More research should also go into testing out more LES models, such as the static Sigma model [70] which has shown to feature improved accuracy over the more computationally involved Dynamic Smagorinsky model [71]. We saw a big difference in performance when using the static Smagorinsky model, without finetuning of the Smagorinsky constant, which indicate that employment of dynamic models may perform better.

During the creation of the helical coil geometries, we found that the extrusion of the employed cross-section profile proved difficult. Since all five sections had to be extruded along a helical path, the sharp twisting angle of C1 caused deformation in the cross-section. Creation of further meshes should therefore be done using a different meshing technique or by utilizing a commercial CAD program that has tighter tolerances and more advanced algorithms for geometry creation. Moreover, the use of hexahedral cells in twisting geometry may not be the optimal choice due to the varying direction of the flow, as shown by the appearance of secondary flow features. Polyhedral meshes may be well suited to this since the geometry of one cell allows for more flexibility of flow direction than that of a hexahedral cell.

We performed the simulations on the coils using wall-modelling which may not be a good choice for this kind of geometry were the boundary layer is not strictly adhering to the characteristics of anisotropic flow. Additionally, the Dean vortices appeared to be close to the wall where wall-modelling were used meaning that since the wall-models may not capture these flows accurately they may have induced inaccuracies on their location and intensity. Further simulations with wall-resolved meshes should be performed to ensure accuracy.

Aforementioned, the mesh resolution in the coils were insufficient due to the decay of turbulence within the coil. This presents a challenge when deciding whether to perform a simulation on a coarse mesh, which has the required resolution but is labor-intensive to refine through multiple iterations, or to maintain a static cell size within the coil. The latter option is preferable if the size of the cells in the coil can be kept constant. One solution to this may be to utilize the Divergence-Free Synthetic Eddy Method boundary condition [67] with an additional extended inlet pipe instead of a periodic domain such that the process is more streamlined. This is especially important for coils with a larger curvature and/or more revolutions due to the effect this has on the dissipation of the turbulence. There should also be performed additional simulations with different LES models to establish possible performance issues when using WALE in such a complicated flow scenario.

Furthermore, the increase in turbulence in the straight pipe outlet creates an unstable flow profile at the boundary. Re-introduction of turbulence was shown experimentally by Viswanath et. al. [5], and should be accounted for in the simulation by further extending the outlet such that a stable profile can develop. Hufnagel et. al. [65] performed simulations with a bent pipe where an outlet length of 15D was deemed to be sufficient, whereas ours was only 5D long.

Appendices

APPENDIX A

Wall shear stress in the O-grid pipe mesh

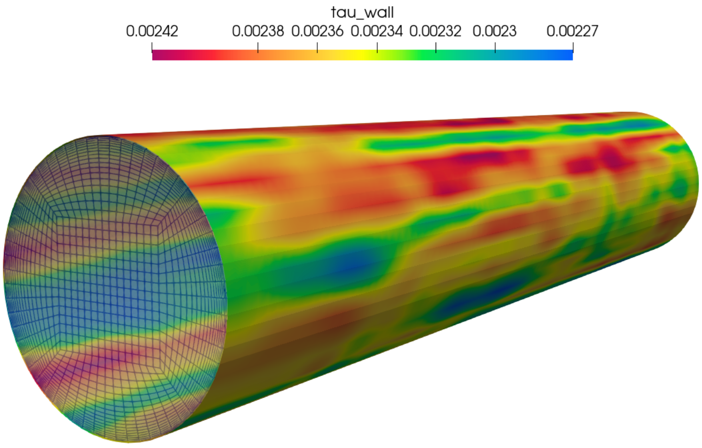

Figure A.1: Wall shear stress from Figure 3.2a.

APPENDIX B

λ_2 criterion

The λ_2 criterion was first proposed by Jeong and Hussain[72] in 1995 as a way to visualize the vorticial motions of turbulence in turbulent flow. The coherent structures (CS) within turbulent flow is of interest for analysis due to their physical significance for convection of quantities.

The λ_2 criterion is defined as follows;

- The velocity gradient tensor is split into its symmetric and anti-symmetric parts such that

$$\frac{\partial u_i}{\partial x_j} = \frac{1}{2}(\frac{\partial u_i}{\partial x_j} + \frac{\partial u_j}{\partial x_i}) + \frac{1}{2}(\frac{\partial u_i}{\partial x_j} - \frac{\partial u_j}{\partial x_i}) = S_{ij} + \Omega_{ij}. \tag{B.1}$$

- Then, by using the Q-definition which is a measure of the amount of rotation compared to strain in the flow we can write that

$$Q = \frac{1}{2}(||\Omega_{ij}||^2 + ||S_{ij}||^2) = -\frac{1}{2}(\lambda_1 + \lambda_2 + \lambda_3), \tag{B.2}$$

  where the eigenvalues of $S_{ij}^2 + \Omega_{ij}^2$ are $\lambda_1 \geq \lambda_2 \geq \lambda_3$ for $Q \geq 0$.

- For incompressible flows, the value for λ_2 is then used to calculate the cubic equation

$$\lambda^3 - Q_i j \lambda - R_i j = 0, \tag{B.3}$$

  where $Q_i j = \frac{1}{2}(\frac{\partial u_i}{\partial x_i})^2$ and $R = det(\frac{\partial u_i}{\partial x_j})$ are two invariants of the velocity gradient tensor.

Using the λ_2 criterion it is possible to set a single threshold to visualize CS, compared to the sensitive parameter for the Q-criterion, as a single value for λ_2 is sufficient to visualize a wide range of structures that satisfies the above criterions.

Bibliography

[1] Vashisth, S., Kumar, V. and Nigam, K. D. 'A review on the potential applications of curved geometries in process industry'. In: *Industrial & Engineering Chemistry Research* vol. 47, no. 10 (2008), pp. 3291–3337.

[2] Coronel, P. and Sandeep, K. 'Heat transfer coefficient in helical heat exchangers under turbulent flow conditions'. In: *International journal of food engineering* vol. 4, no. 1 (2008).

[3] Dean, W. R. 'XVI. Note on the motion of fluid in a curved pipe'. In: *The London, Edinburgh, and Dublin Philosophical Magazine and Journal of Science* vol. 4, no. 20 (1927), pp. 208–223.

[4] Taylor, G. I. 'The criterion for turbulence in curved pipes'. In: *Proceedings of the Royal Society of London. Series A, Containing Papers of a Mathematical and Physical Character* vol. 124, no. 794 (1929), pp. 243–249.

[5] Viswanath, P., Narasimha, R. and Prabhu, A. 'Visualization of relaminarizing flows.' In: *Journal of the Indian Institute of Science* vol. 60, no. 3 (1978), p. 159.

[6] Sreenivasan, K. and Strykowski, P. 'Stabilization effects in flow through helically coiled pipes'. In: *Experiments in Fluids* vol. 1, no. 1 (1983), pp. 31–36.

[7] Lin, C. and Ebadian, M. 'The effects of inlet turbulence on the development of fluid flow and heat transfer in a helically coiled pipe'. In: *International Journal of Heat and Mass Transfer* vol. 42, no. 4 (1999), pp. 739–751.

[8] Noorani, A., El Khoury, G. and Schlatter, P. 'Evolution of turbulence characteristics from straight to curved pipes'. In: *International journal of heat and fluid flow* vol. 41 (2013), pp. 16–26.

[9] Kalpakli, A. 'Experimental study of turbulent flows through pipe bends'. KTH Royal Institute of Technology, 2012.

[10] Tang, L., Tang, Y. and Parameswaran, S. 'A numerical study of flow characteristics in a helical pipe'. In: *Advances in Mechanical Engineering* vol. 8, no. 7 (2016), p. 1687814016660242.

[11] Yamamoto, K. 'Numerical Investigation of Turbulent Flow in Helically Coiled Pipes'. MA thesis. 2022.

[12] Bush, R. H. et al. 'Recommendations for future efforts in RANS modeling and simulation'. In: *AIAA scitech 2019 forum*. 2019, p. 0317.

[13] Versteeg, H. K. and Malalasekera, W. *An introduction to computational fluid dynamics: the finite volume method*. Pearson education, 2007.

[14] Rumsey, C. *Turbulence modeling resource*. https://turbmodels.larc.nasa.gov/. Accessed: 02-June-2023. Mar. 2023.

[15] Martins, N. M. et al. 'Velocity-distribution in pressurized pipe flow using CFD: Accuracy and mesh analysis'. In: *Computers & Fluids* vol. 105 (2014), pp. 218–230.

[16] Ballesteros, M., Ratkovich, N. and Pereyra, E. 'Analysis and Modeling of Liquid Holdup in Low Liquid Loading Two-Phase Flow Using Computational Fluid Dynamics and Experimental Data'. In: *Journal of Energy Resources Technology* vol. 143, no. 1 (2021).

[17] Hernandez-Perez, V., Abdulkadir, M. and Azzopardi, B. 'Grid generation issues in the CFD modelling of two-phase flow in a pipe'. In: *The Journal of Computational Multiphase Flows* vol. 3, no. 1 (2011), pp. 13–26.

[18] Wang, Z. et al. 'An entropy-viscosity large eddy simulation study of turbulent flow in a flexible pipe'. In: *Journal of Fluid Mechanics* vol. 859 (2019), pp. 691–730.

[19] El Khoury, G. K. et al. 'Direct numerical simulation of turbulent pipe flow at moderately high Reynolds numbers'. In: *Flow, turbulence and combustion* vol. 91 (2013), pp. 475–495.

[20] ESI Group. *OpenFOAM*. https://www.openfoam.com/. Version 2106. 1st June 2021.

[21] IdealSimulations. *CFD modelling of a turbulent jet using different approaches*. https://www.idealsimulations.com/resources/turbulence-models-in-cfd/. Accessed: 26-May-2023. 2020.

[22] Reynolds, O. 'IV. On the dynamical theory of incompressible viscous fluids and the determination of the criterion'. In: *Philosophical transactions of the royal society of london.(a.)*, no. 186 (1895), pp. 123–164.

[23] Pope, S. *Turbulent Flows*. Cambridge University Press, 2010.

[24] Lesieur, M., Métais, O. and Comte, P. *Large-Eddy Simulations of Turbulence*. Cambridge University Press, 2005.

[25] Denaro, F. M. 'CFD course: The basic of implicit-based filtering in Large Eddy Simulation'. In: (Sept. 2021).

[26] Denaro, F. M. 'What does Finite Volume-based implicit filtering really resolve in Large-Eddy Simulations?' In: *Journal of Computational Physics* vol. 230, no. 10 (2011), pp. 3849–3883.

[27] Leonard, A. 'Energy cascade in large-eddy simulations of turbulent fluid flows'. In: *Advances in geophysics*. Vol. 18. Elsevier, 1975, pp. 237–248.

[28] Boussinesq, J. V. *Essai sur la theorie des eaux courantes*. Impr. nationale, 1877.

[29] Smagorinsky, J. 'General circulation experiments with the primitive equations: I. The basic experiment'. In: *Monthly weather review* vol. 91, no. 3 (1963), pp. 99–164.

[30] Nicoud, F. and Ducros, F. ‘Subgrid-scale stress modelling based on the square of the velocity gradient tensor’. In: *Flow, turbulence and Combustion* vol. 62, no. 3 (1999), pp. 183–200.

[31] Lilly, D. K. ‘The representation of small-scale turbulence in numerical simulation experiments’. In: *Proc. IBM Sci. Comput. Symp. on Environmental Science*. 1967, pp. 195–210.

[32] Mukha, T., Rezaeiravesh, S. and Liefvendahl, M. ‘A library for wall-modelled large-eddy simulation based on OpenFOAM technology’. In: *Computer Physics Communications* vol. 239 (2019), pp. 204–224.

[33] Yoshizawa, A. and Horiuti, K. ‘A statistically-derived subgrid-scale kinetic energy model for the large-eddy simulation of turbulent flows’. In: *Journal of the Physical Society of Japan* vol. 54, no. 8 (1985), pp. 2834–2839.

[34] Pereira, F. S. et al. ‘Toward predictive RANS and SRS computations of turbulent external flows of practical interest’. In: *Archives of Computational Methods in Engineering* vol. 28 (2021), pp. 3953–4029.

[35] Jasak, H. ‘Error analysis and estimation for the finite volume method with applications to fluid flows.’ In: (1996).

[36] Issa, R. I. ‘Solution of the implicitly discretised fluid flow equations by operator-splitting’. In: *Journal of computational physics* vol. 62, no. 1 (1986), pp. 40–65.

[37] Ltd., O. *Pressure-velocity algorithms.* https://www.openfoam.com/documentation/guides/latest/doc/guide-fv-solution-pressure-velocity-algorithms.html. Accessed: 02-June-2023. 2023.

[38] aokomoriuta. *Law of the wall.* https://commons.wikimedia.org/w/index.php?curid=15672321. Accessed: 02-March-2023. 2011.

[39] Chapman, D. R. ‘Computational aerodynamics development and outlook’. In: *AIAA journal* vol. 17, no. 12 (1979), pp. 1293–1313.

[40] Choi, H. and Moin, P. ‘Grid-point requirements for large eddy simulation: Chapman’s estimates revisited’. In: *Physics of fluids* vol. 24, no. 1 (2012), p. 011702.

[41] Bradshaw, P. and Huang, G. P. ‘The law of the wall in turbulent flow’. In: *Proceedings of the Royal Society of London. Series A: Mathematical and Physical Sciences* vol. 451, no. 1941 (1995), pp. 165–188.

[42] Spalding, D. et al. ‘A single formula for the law of the wall’. In: *Journal of Applied Mechanics* vol. 28, no. 3 (1961), pp. 455–458.

[43] Mandal, B. and Mazumdar, H. P. ‘The importance of the law of the wall’. In: *International Journal of Applied Mechanics and Engineering* vol. 20, no. 4 (2015), pp. 857–869.

[44] Slotnick, J. P. et al. *CFD vision 2030 study: a path to revolutionary computational aerosciences.* Tech. rep. 2014.

[45] De Villiers, E. ‘The potential of large eddy simulation for the modeling of wall bounded flows’. In: *Imperial College of Science, Technology and Medicine* (2006).

[46] Moukalled, F. et al. *The finite volume method.* Springer, 2016.

[47] Jiménez, J. ‘The physics of wall turbulence’. In: *Physica A: Statistical Mechanics and its Applications* vol. 263, no. 1-4 (1999), pp. 252–262.

[48] Feldmann, D. and Avila, M. ‘Overdamped large-eddy simulations of turbulent pipe flow up to Reτ= 1500’. In: *Journal of Physics: Conference Series*. Vol. 1001. 1. IOP Publishing. 2018, p. 012016.

[49] Piomelli, U. and Balaras, E. ‘Wall-layer models for large-eddy simulations’. In: *Annual review of fluid mechanics* vol. 34, no. 1 (2002), pp. 349–374.

[50] Chernyshenko, S. and Baig, M. ‘The mechanism of streak formation in near-wall turbulence’. In: *Journal of Fluid Mechanics* vol. 544 (2005), pp. 99–131.

[51] Jeong, J. et al. ‘Coherent structures near the wall in a turbulent channel flow’. In: *Journal of Fluid Mechanics* vol. 332 (1997), pp. 185–214.

[52] Smith, F. T. ‘Fluid flow into a curved pipe’. In: *Proceedings of the Royal Society of London. A. Mathematical and Physical Sciences* vol. 351, no. 1664 (1976), pp. 71–87.

[53] Das, S. K. ‘Water flow through helical coils in turbulent condition’. In: *Advances in Engineering Fluid Mechanics: Multiphase Reactor and Polymerization System Hydrodynamics*. Elsevier, 1996, pp. 379–403.

[54] Pan, C., Zhou, Y. and Wang, J. ‘CFD study of heat transfer for oscillating flow in helically coiled tube heat-exchanger’. In: *Computers & chemical engineering* vol. 69 (2014), pp. 59–65.

[55] Huttl, T. and Friedrich, R. ‘Influence of curvature and torsion on turbulent flow in helically coiled pipes’. In: *International Journal of Heat and Fluid Flow* vol. 21, no. 3 (2000), pp. 345–353.

[56] Ciofalo, M., Di Liberto, M. and Marotta, G. ‘On the influence of curvature and torsion on turbulence in helically coiled pipes’. In: *Journal of Physics: Conference Series* vol. 501, no. 1 (2014), pp. 12–25.

[57] Lozano-Durán, A. and Bae, H. J. ‘Error scaling of large-eddy simulation in the outer region of wall-bounded turbulence’. In: *Journal of computational physics* vol. 392 (2019), pp. 532–555.

[58] Kawai, S. and Larsson, J. ‘Wall-modeling in large eddy simulation: Length scales, grid resolution, and accuracy’. In: *Physics of fluids* vol. 24, no. 1 (2012).

[59] Bull, J. R. and Jameson, A. ‘Explicit filtering and exact reconstruction of the sub-filter stresses in large eddy simulation’. In: *Journal of Computational Physics* vol. 306 (2016), pp. 117–136.

[60] Hayamizu, Y. et al. ‘Experimental study of the flow in helical circular pipes: Torsion effect on the flow velocity and turbulence’. In: *Journal of Thermal Science* vol. 17 (2008), pp. 193–198.

[61] Nashine, P. and Singh, T. S. ‘Effect of dean number on the heat transfer characteristics of a helical coil tube with variable velocity & pressure inlet’. In: *Journal of Thermal Engineering* vol. 6, no. 2 (2020), pp. 128–139.

[62] Ferng, Y., Lin, W. and Chieng, C. ‘Numerically investigated effects of different Dean number and pitch size on flow and heat transfer characteristics in a helically coil-tube heat exchanger’. In: *Applied Thermal Engineering* vol. 36 (2012), pp. 378–385.

[63] Nusselt, W. ‘Die oberflachenkondensation des wasserdamphes’. In: *VDI-Zs* vol. 60 (1916), p. 541.

[64] Rütten, F., Schröder, W. and Meinke, M. ‘Large-eddy simulation of low frequency oscillations of the Dean vortices in turbulent pipe bend flows’. In: *Physics of Fluids* vol. 17, no. 3 (2005).

[65] Hufnagel, L. et al. ‘The three-dimensional structure of swirl-switching in bent pipe flow’. In: *Journal of Fluid Mechanics* vol. 835 (2018), pp. 86–101.

[66] Tunstall, M. and Harvey, J. ‘On the effect of a sharp bend in a fully developed turbulent pipe-flow’. In: *Journal of Fluid Mechanics* vol. 34, no. 3 (1968), pp. 595–608.

[67] Jarrin, N. et al. ‘A synthetic-eddy-method for generating inflow conditions for large-eddy simulations’. In: *International Journal of Heat and Fluid Flow* vol. 27, no. 4 (2006), pp. 585–593.

[68] Li, Y., Wang, W. and Okaze, T. ‘Evaluation of polyhedral mesh performance for large-eddy simulations of flow around an isolated building within an unstable boundary layer’. In: *Building and Environment* vol. 235 (2023), p. 110207.

[69] Wang, W., Cao, Y. and Okaze, T. ‘Comparison of hexahedral, tetrahedral and polyhedral cells for reproducing the wind field around an isolated building by LES’. In: *Building and Environment* vol. 195 (2021), p. 107717.

[70] Nicoud, F. et al. ‘Using singular values to build a subgrid-scale model for large eddy simulations’. In: *Physics of fluids* vol. 23, no. 8 (2011).

[71] Germano, M. et al. ‘A dynamic subgrid-scale eddy viscosity model’. In: *Physics of Fluids A: Fluid Dynamics* vol. 3, no. 7 (1991), pp. 1760–1765.

[72] Jeong, J. and Hussain, F. ‘On the identification of a vortex’. In: *Journal of fluid mechanics* vol. 285 (1995), pp. 69–94.